

École doctorale n° 364 : Sciences Fondamentales et Appliquées

## Doctorat ParisTech

### THÈSE

pour obtenir le grade de docteur délivré par

**l'École Nationale Supérieure des Mines de Paris**

**Spécialité doctorale “Science et Génie des Matériaux”**

*présentée et soutenue publiquement par*

**Ali SAAD**

le xx septembre 2015

## NUMERICAL MODELLING OF MACROSEGREGATION FORMED DURING SOLIDIFICATION WITH SHRINKAGE USING A LEVEL SET APPROACH

Directeurs de thèse: **Michel BELLET**  
**Charles-André GANDIN**

### Jury

<b>M. Blablabla</b> ,	Professeur, MINES ParisTech	Rapporteur
<b>M. Blablabla</b> ,	Professeur, Arts Et Métiers ParisTech	Rapporteur
<b>M. Blablabla</b> ,	Chargé de recherche, ENS Cachan	Examinateur
<b>M. Blablabla</b> ,	Danseuse, en freelance	Examinateur
<b>M. Blablabla</b> ,	Ingénieur, MIT	Examinateur

T  
H  
E  
S  
S  
E

MINES ParisTech  
Centre de Mise en Forme des Matériaux (CEMEF)  
UMR CNRS 7635, F-06904 Sophia Antipolis, France



---

## **Acknowledgement**

Dedicated to humanity ...



# Contents

<b>1 General Introduction</b>	<b>1</b>
1.1 Solidification notions . . . . .	2
1.1.1 Solute partitioning . . . . .	2
1.1.2 Dendritic growth . . . . .	4
1.1.3 Mush permeability . . . . .	6
1.2 Macrosegregation . . . . .	7
1.2.1 Liquid thermosolutal convection . . . . .	8
1.2.2 Solidification shrinkage . . . . .	9
1.2.3 Movement of equiaxed grains . . . . .	9
1.2.4 Solid deformation . . . . .	9
1.3 Other defects . . . . .	9
1.4 Industrial Worries . . . . .	11
1.5 Project context and objectives . . . . .	12
1.5.1 Context . . . . .	12
1.5.2 Objectives and outline . . . . .	13
<b>2 Modelling Review</b>	<b>19</b>
2.1 Modelling macrosegregation . . . . .	20
2.1.1 Macroscopic solidification model: monodomain . . . . .	21
2.2 Eulerian and Lagrangian motion description . . . . .	27
2.2.1 Overview . . . . .	27
2.2.2 Interface capturing . . . . .	30
2.3 Solidification models with level set . . . . .	30
2.4 The level set method . . . . .	31
2.4.1 Diffuse interface . . . . .	32
2.4.2 Mixing Laws . . . . .	34
2.5 Interface motion . . . . .	35
2.5.1 Level set transport . . . . .	36

## Contents

---

2.5.2	Level set regularisation . . . . .	37
2.6	Mesh adaptation . . . . .	41
2.6.1	Metrics and anisotropy . . . . .	41
2.6.2	<i>Remesh2</i> : Interface remeshing . . . . .	43
2.6.3	<i>Remesh4</i> : Multi-criteria remeshing . . . . .	44
<b>3</b>	<b>Energy balance with thermodynamic tabulations</b>	<b>47</b>
3.1	State of the art . . . . .	48
3.2	Thermodynamic considerations . . . . .	49
3.2.1	Volume averaging . . . . .	49
3.2.2	The temperature-enthalpy relationship . . . . .	50
3.2.3	Tabulation of properties . . . . .	50
3.3	Numerical method . . . . .	52
3.3.1	Enthalpy-based approach . . . . .	56
3.3.2	Temperature-based approach . . . . .	56
3.3.3	Convergence . . . . .	57
3.4	Validation . . . . .	58
3.5	Application: multicomponent alloy solidification . . . . .	61
3.5.1	Tabulations . . . . .	63
3.5.2	Discussion . . . . .	65
<b>4</b>	<b>Macrosegregation with liquid metal motion</b>	<b>71</b>
4.1	Introduction . . . . .	73
4.2	Formulation stability . . . . .	73
4.2.1	Stable mixed finite elements . . . . .	73
4.2.2	Variational multiscale (VMS) . . . . .	74
4.3	Navier-Stokes solver . . . . .	75
4.3.1	Strong and weak formulations . . . . .	75
4.3.2	Stabilisation parameters . . . . .	79
4.3.3	Implementation . . . . .	80
4.4	Application to multicomponent alloys . . . . .	81
4.4.1	<i>Tsolver</i> validation with fluid flow . . . . .	81
4.4.2	Results . . . . .	84
4.5	Macroscopic prediction of channel segregates . . . . .	87
4.5.1	Introduction . . . . .	87
4.5.2	Experimental work . . . . .	89
4.5.3	Macroscopic scale simulations . . . . .	89
4.6	Meso-Macro prediction of channel segregates . . . . .	97

4.6.1	Numerical method . . . . .	97
4.6.2	Configuration . . . . .	98
4.6.3	Effect of vertical temperature gradient . . . . .	103
4.6.4	Effect of cooling rate . . . . .	105
4.6.5	Effect of lateral temperature gradient . . . . .	107
4.6.6	Mono-grain freckles . . . . .	108
<b>5</b>	<b>Macrosegregation with solidification shrinkage</b>	<b>111</b>
5.1	Solidification shrinkage . . . . .	113
5.2	Choice of interface tracking . . . . .	113
5.3	Multidomain formalism . . . . .	115
5.3.1	Assumptions . . . . .	116
5.4	FE partitioned model . . . . .	117
5.4.1	In the metal . . . . .	118
5.4.2	In the air . . . . .	122
5.5	FE monolithic model . . . . .	124
5.5.1	Monolithic equations . . . . .	124
5.5.2	Darcy term in the air . . . . .	127
5.5.3	Interface motion and stability . . . . .	128
5.6	1D application: solidification with inverse segregation . . . . .	131
5.6.1	Geometry and boundary conditions . . . . .	131
5.6.2	Shrinkage without macrosegregation . . . . .	132
5.6.3	Shrinkage with macrosegregation . . . . .	141
5.7	2D application: controlled solidification benchmark . . . . .	149
5.7.1	Absence of convection . . . . .	150
5.8	3D application: reduced-gravity solidification . . . . .	150
5.8.1	Previous work . . . . .	150
5.8.2	Computational configuration . . . . .	153
5.8.3	Texus binary alloy . . . . .	160
5.8.4	Texus ternary and quaternary alloys . . . . .	168
5.8.5	TODO . . . . .	169
<b>Bibliography</b>		<b>171</b>

## **Contents**

---

## List of Acronyms

---

Acronym	Standing for
ALE	Arbitrary Lagrangian-Eulerian
BTR	Brittle temperature range
CAFD	Cellular Automata Finite Difference
CAFE	Cellular Automata Finite Element
CBB	Circumventing Babuška-Brezzi
CCEMLCC	Chill Cooling for the Electro-Magnetic Levitator in relation with Continuous Casting of steel
CEMEF	Centre de Mise en Forme des Matériaux
CFL	Courant–Friedrichs–Lewy
C.FL	Computing and FLuids
CSF	Continuum Surface Force
DLR	Deutsches Zentrum für Luft- und Raumfahrt
DSPG	Darcy-Stabilising/Petrov-Galerkin
EML	Electromagnetic levitation
ESA	European Space Agency
FEM	Finite Element Method
FVM	Finite Volume Method
GMAW	Gas Metal Arc Welding
ISS	International Space Station
IWT	Institut für Werkstofftechnik
LHS	Left-hand side
LSIC	Least squares on incompressibility constraint
LSM	Level set method
MAC	Marker-and-cell
PF	Phase field
PSPG	Pressure-Stabilising/Petrov-Galerkin
RHS	Right-hand side
RUB	Ruhr Universität Bochum
RVE	Representative Elementary Volume
SBB	Satisfying Babuška-Brezzi
SUPG	Streamline-Upwind/Petrov-Galerkin
VMS	Variational MultiScale
VOF	Volume Of Fluid

---

## **Contents**

---

## **Contents**

---

# Chapter 3

## Energy balance with thermodynamic tabulations

### Contents

---

<b>3.1 State of the art . . . . .</b>	<b>48</b>
<b>3.2 Thermodynamic considerations . . . . .</b>	<b>49</b>
3.2.1 Volume averaging . . . . .	49
3.2.2 The temperature-enthalpy relationship . . . . .	50
3.2.3 Tabulation of properties . . . . .	50
<b>3.3 Numerical method . . . . .</b>	<b>52</b>
3.3.1 Enthalpy-based approach . . . . .	56
3.3.2 Temperature-based approach . . . . .	56
3.3.3 Convergence . . . . .	57
<b>3.4 Validation . . . . .</b>	<b>58</b>
<b>3.5 Application: multicomponent alloy solidification . . . . .</b>	<b>61</b>
3.5.1 Tabulations . . . . .	63
3.5.2 Discussion . . . . .	65

---

### 3.1 State of the art

To model macrosegregation during solidification, a minimum of four conservation equations are necessary: conservation of mass, momentum, chemical species and energy. The phase change literature contains a wealth of numerical methods to solve energy conservation in solidifying alloys. A comprehensive overview of these methods is given by [Swaminathan and Voller \[1993\]](#).

The corresponding equation associates the total average enthalpy to the temperature via intrinsic alloy properties, such as the heat capacity of the phases and the latent heat associated with the phase transformations. However, in the course of solidification and while macrosegregation is taking place, these properties change because the average composition may vary significantly: the transformation paths are thus modified, as well as the phases' composition and heat capacity. Similarly, the latent heat of phase transformations is not a mere constant that could be distributed as a function of the phase fractions assuming only temperature-dependent phases' properties, as often found in the literature [\[Bellet et al. 2009\]](#). It is thus impossible to establish a priori the dependence of the enthalpy with respect to temperature when macrosegregation alters the average composition, even in the case of full thermodynamic equilibrium between phases.

In this chapter, we discuss a suitable numerical scheme based on an enthalpy method, already used in the literature to alleviate this macrosegregation-related problem [\[Swaminathan and Voller 1993; Carozzani et al. 2013\]](#). Later on, we introduce a modified formulation, using the effective heat capacity method that increases the original scheme's efficiency.

This chapter introduces an enthalpy method that makes use of a temperature-based solver. It uses tabulated thermodynamic quantities (solidification paths, phases' enthalpy and composition) in a range of average compositions and temperatures as found in the literature [\[Doré et al. 2000; Thuinet and Combeau 2004; Du et al. 2007\]](#), with the aim of evaluating the total average enthalpy as well as the effective heat capacity. The novelty of the modified method resides in the use of thermodynamic tabulations without losing the advantages of the previous method, thus yielding faster computation times while maintaining a good accuracy.

## 3.2 Thermodynamic considerations

### 3.2.1 Volume averaging

The volume averaging technique, presented in [section 2.1.1](#), is considered when solving the energy equation in the presence of macrosegregation. The reason is that phase properties and distributions varying with the average composition, have a great impact on the average thermal properties, and hence on the overall heat transfer in the system. We recall the basic equation:

$$\langle \psi \rangle = \sum_{\phi} g^{\phi} \langle \psi \rangle^{\phi} \quad (3.1)$$

where  $g^{\phi}$  denotes the volume fraction of phase  $\phi$  in the RVE. It should be emphasized that the averaging technique applies to virtually all thermodynamic volumetric variables (enthalpy, density ...). Among these variables, the temperature is also considered to be uniform in the RVE.

Applying the volume averaging technique to the energy conservation principle along with interfacial balances between the phases, results in the following averaged equation [[Rappaz et al. 2003](#)]:

$$\frac{\partial \langle \rho h \rangle}{\partial t} + \nabla \cdot \langle \rho h \vec{v} \rangle = \nabla \cdot (\langle \kappa \rangle \vec{\nabla} T) + \langle \dot{Q}_V \rangle \quad (3.2)$$

where  $\rho$  stands for the density,  $h$  the mass enthalpy,  $\vec{v}$  the velocity field,  $\kappa$  the thermal conductivity,  $T$  the temperature and  $\dot{Q}_V$  a possible volumetric heat source. [Equation \(3.2\)](#) is the standard averaged form of the energy conservation equation used in non-stationary phase change problems.

It is clear that the nature of the temperature-enthalpy relationship plays a central role when formulating the resolution strategy of this nonlinear equation. Generally, it is admitted that, depending on the resolution strategy, it is necessary to express enthalpy as a function of temperature or vice-versa, together with associated partial derivatives,  $\frac{d\langle \rho h \rangle}{dT}$  or  $\frac{dT}{d\langle \rho h \rangle}$ .

It is noted that in the FEM context, the RVE is represented by a node in a finite element, so for instance the temperature in a RVE is denoted  $T_j$  henceforth, where  $j$  represents the index of the node localising the RVE.

### 3.2.2 The temperature-enthalpy relationship

In solidification problems, additional variables are involved in [eq. \(3.1\)](#) and [eq. \(3.2\)](#), like the transformation path that defines the history of the phase fractions, as well as the average chemical composition  $\langle w_i \rangle$ ,  $i$  being the index of the chemical species (only the solutes are considered). The temperature-enthalpy relation averaged over the phases in a given RVE writes:

$$\langle \rho h \rangle = \sum_{\phi} g^{\phi}_{(T, \langle w_i \rangle \dots)} \langle \rho \rangle^{\phi}_{(T, \langle w_i \rangle^{\phi} \dots)} \langle h \rangle^{\phi}_{(T, \langle w_i \rangle^{\phi} \dots)} \quad (3.3)$$

Note that the volume average enthalpy is approximated by the product  $\langle \rho h \rangle^{\phi} = \langle h \rangle^{\phi} \langle \rho \rangle^{\phi}$  in the current work. As stated in the introduction, it becomes clear from [eq. \(3.3\)](#) that phase properties, i.e. average phase density,  $\langle \rho \rangle^{\phi}$  and enthalpy,  $\langle h \rangle^{\phi}$ , are temperature and composition dependent. This equation is the key to convert the average volume enthalpy to temperature (through a procedure named *H2T*) or vice-versa (*T2H*). The values of the different phase fractions  $g^{\phi}$  (solidification path) and phase enthalpies  $\langle \rho h \rangle^{\phi}$  are thus needed to close the relation.

### 3.2.3 Tabulation of properties

The complexity of performing a thermodynamic conversion is directly linked to the simplicity of determining the alloy properties, namely the phase fractions and both phase densities and enthalpies. In the case of binary alloys and with several assumptions with respect to the system (e.g., linear monovariant lines in temperature-composition relationships of the phase diagram, constant heat capacity of phases and constant latent heat of transformations, equilibrium approximations between phases) analytical calculations are often used to determine the phase fractions and phase compositions. Nevertheless, analytical relations are more complex or even impossible to derive in the case of multicomponent alloys ( $i > 1$ ), or even for binary alloys with multiple phase transformations (e.g. peritectic and eutectic reactions) with a nonlinear phase diagram.

To overcome this problem, one can resort to thermodynamic databases and phase equilibrium calculations to tabulate the transformation paths and the phase densities and enthalpies for a given range of temperatures and average compositions. It is a handy solution for two main reasons: first, the conversion is merely a binary search in a table; secondly, it is a simple solution for coupling with macrosegregation. In this way, phase fractions  $g^{\phi}$  are tabulated as functions of temperature and average composition, while for each phase  $\phi$  the mass enthalpy,  $\langle h \rangle^{\phi}$ , and the density,  $\langle \rho \rangle^{\phi}$ , are

## 3.2. Thermodynamic considerations

---

tabulated as functions of temperature and phase intrinsic average compositions  $\langle w_i \rangle^\phi$ , as well as other possible parameters.

**Table 3.1** summarizes the steps in order to perform a temperature-to-enthalpy ( $T2H$ ) conversion using the predefined tabulation approach. In step 1, the transformation path is acquired for each average composition,  $\langle w_i \rangle$ , and temperature,  $T$ , to determine the list of phases, their volume fractions  $g^\phi$  and their intrinsic compositions  $\langle w_i \rangle^\phi$ , assuming full equilibrium. In step 2, the phase enthalpy  $\langle h \rangle^\phi$  and density  $\langle \rho \rangle^\phi$  are determined by searching for the temperature and the already known phase composition  $\langle w_i \rangle^\phi$ . In step 3, the average volume enthalpy is computed from the volume fraction, density and mass enthalpy of phases using [eq. \(3.3\)](#). A flowchart explaining  $T2H$  conversion steps is given in [fig. 3.1](#).

**Table 3.1** – Tabulation processing for a  $T2H$  procedure

Step Number	1	2	3
<b>Inputs</b>	$T, \langle w_i \rangle$	$T, \langle w_i \rangle^\phi$	$g^\phi, \langle \rho \rangle^\phi \langle h \rangle^\phi$
<b>Outputs</b>	$g^\phi, \langle w_i \rangle^\phi$	$\langle \rho \rangle^\phi, \langle h \rangle^\phi$	$\langle ph \rangle$ ( <a href="#">eq. (3.3)</a> )

The methodology to build the tabulations is straightforward. It is based on two main scans. On the one hand, intervals for the variation of the average composition  $\langle w_i \rangle$  are chosen from the known alloy composition. These variations have to cover the extreme values adopted during the simulation, which are not known a priori. An interval is also selected for the variation of temperature. The latter is easier to determine as it usually starts from the initial melt temperature and goes down to the room temperature in a standard casting simulation. For each mapping of composition and temperature, a thermodynamic equilibrium state is computed. The outputs are the number of phases encountered, together with their fraction and intrinsic compositions. On the other hand, for each phase, a scan of the intrinsic composition and temperature is made to compute the intrinsic properties. The same temperature interval and step as defined earlier are used.

Regarding the enthalpy-to-temperature conversion ( $H2T$ ) shown in the flowchart in [fig. 3.2](#), a backward iterative  $T2H$  search is performed. For a known composition  $\langle w_i \rangle$ , denoting  $(\tau)$  the iteration index to convert the enthalpy  $H_{\text{input}}$ , we start with an initial guess for temperature  $T^{(\tau=0)}$  then convert it to an enthalpy  $H^{(\tau=0)}$  with the  $T2H$  conversion. Using an appropriate nonlinear algorithm (Brent is the most versatile in our case), we aim at minimizing the following scalar residual:  $R_H = |H_{\text{input}} - H^{(\tau)}|$ . Once the algorithm has converged, the temperature  $T^{(\tau)}$  is the result of the  $H2T$  conversion. It is inferred that the first conversion ( $T2H$ ) is a direct one whereas the latter ( $H2T$ ) is

### Chapter 3. Energy balance with thermodynamic tabulations

---

indirect and requires a series of iterative steps; each step being a single  $T2H$  resolution. In other words, a  $H2T$  conversion is a backward search for a temperature, hence it is slower. This conversion's speed lag is exacerbated when tabulations increase in size (e.g. large number of temperature and composition steps) and complexity (e.g., multi-component industrial alloys used in casting), since the search gets more complicated with the increasing number of input columns (one column for each alloying element).

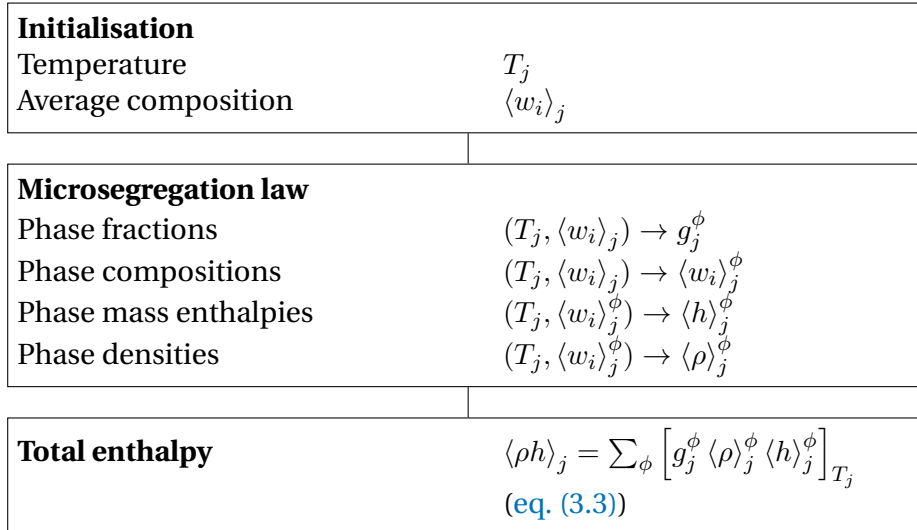


**Fig. 3.1** – Algorithm for a single temperature to enthalpy ( $T2H$ ) conversion at node  $j$ .

### 3.3 Numerical method

The finite element method is used to solve the energy conservation as expressed by [eq. \(3.2\)](#). A test function  $\mathcal{W}$  belonging to the Hilbertian Sobolev space  $\mathcal{H}^1(\Omega_E)$  of continuous integrable test functions is used to formulate the integral variational form of [eq. \(3.2\)](#) [[Süli 2000](#)]. A Fourier boundary condition is considered on the domain boundary  $\partial\Omega_E$ . The domain  $\Omega$  is discretised using first-order linear simplexes,  $\Omega_E$ , defined by their number of local nodes, NbLoc: triangles in 2D with NbLoc=3 and tetrahedra in 3D with NbLoc=4. The outcome is a residual that we aim to minimize so that the conservation principle is satisfied. Therefore, the weak form writes:

$$\begin{aligned} \forall \mathcal{W} \in M = \{u \in \mathcal{H}^1(\Omega_E)\} \\ \int_{\Omega_E} \mathcal{W} \frac{\partial H}{\partial t} dV + \int_{\Omega_E} \mathcal{W} \left\langle \vec{v}^l \right\rangle \cdot \vec{\nabla} \langle \rho h \rangle^l dV - \int_{\Omega_E} \mathcal{W} \nabla \cdot (\langle \kappa \rangle \vec{\nabla} T) dV - \int_{\Omega_E} \mathcal{W} \left\langle \dot{Q}_V \right\rangle dV = 0 \end{aligned} \quad (3.4)$$

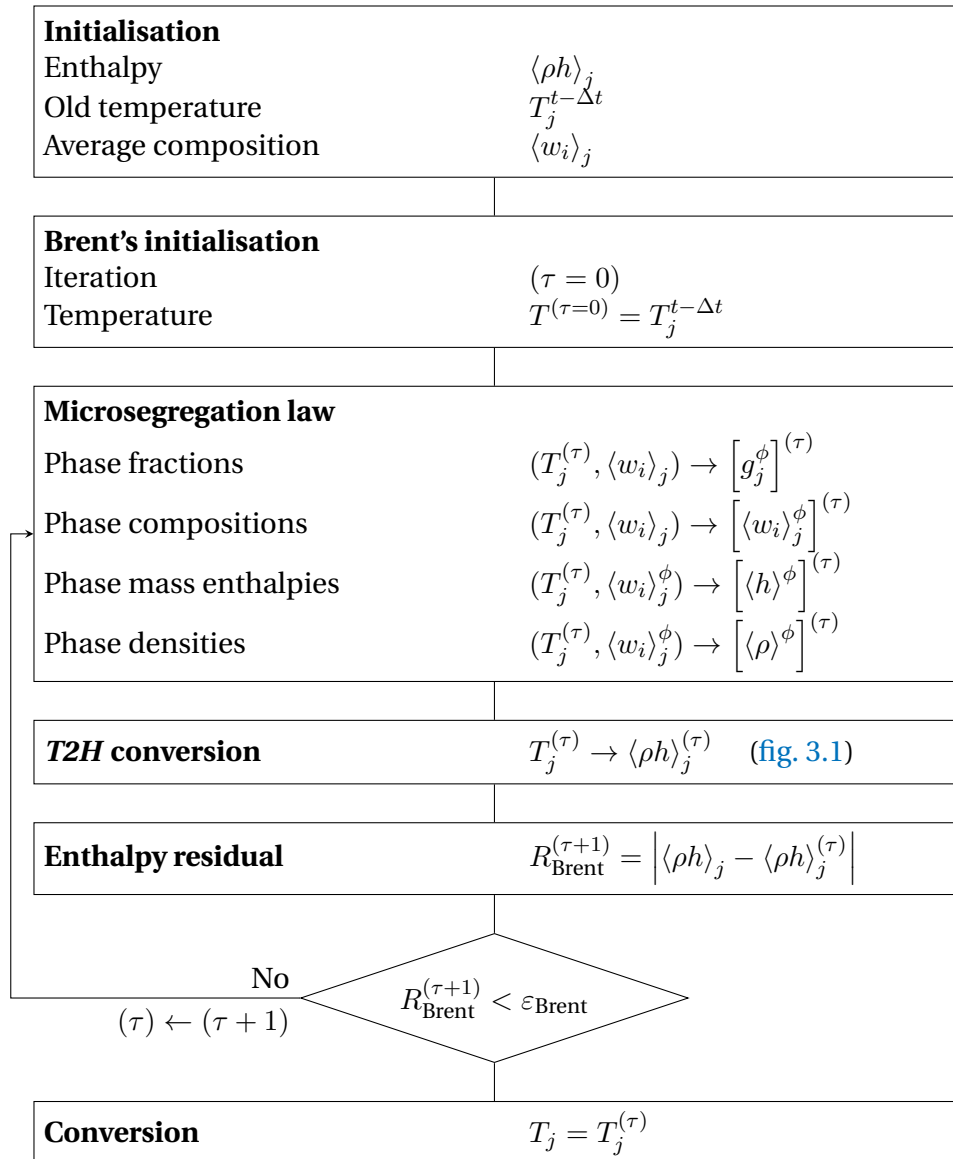


**Fig. 3.2** – Algorithm for a single enthalpy to temperature ( $H2T$ ) conversion at node  $j$ .

### Chapter 3. Energy balance with thermodynamic tabulations

---

where  $H = \rho h$  is the volumetric enthalpy, introduced to simplify notations in the following. Furthermore, we assumed a static solid phase and an incompressible liquid phase, which allowed recasting the second term of [eq. \(3.2\)](#) into  $\langle \vec{v}^l \rangle \cdot \vec{\nabla} \langle \rho h \rangle^l$ .  $\langle \rho h \rangle^l = \langle \rho \rangle^l \langle h \rangle^l$  is not main variable of the energy conservation equation's weak form, [eq. \(3.4\)](#). Therefore we express it as a function of temperature, which is related to the main variable via the enthalpy-temperature relation:

$$\vec{\nabla} \langle \rho h \rangle^l = \vec{\nabla} (\langle \rho \rangle^l \langle h \rangle^l) = \langle \rho \rangle^l C_p^l \vec{\nabla} T \quad (3.5)$$

where  $C_p^l$  is the mass heat capacity of the liquid phase. Ideally, this value should be taken directly from the thermodynamic database if it is available. Otherwise, it can be derived by differentiation of the tabulated liquid mass enthalpy with respect to temperature. In this work,  $C_p^l$  is considered constant, equal to the alloy's initial mass heat capacity. The steps for discretising in time and space [eq. \(3.4\)](#) are well detailed in some text books like [Rappaz et al. \[2003\]](#). As for enthalpy and temperature, they are spatially discretised in each simplex using interpolations functions  $\mathcal{P}$ , thus defining the nodal values  $H_j$  and  $T_j$ , respectively:

$$H = \sum_{j=1}^{\text{NbLoc}} \mathcal{P}_j H_j \quad (3.6)$$

$$T = \sum_{j=1}^{\text{NbLoc}} \mathcal{P}_j T_j \quad (3.7)$$

The Galerkin formulation gives the expression for the residual contribution at a mesh node  $i$  (here  $i$  is not the usual solute index) for time step  $t$  in a local element  $\Omega_E$ :

$$(R_i^E)^t = \mathcal{M}_{ij}^E (H_j^t - H_j^{t-\Delta t}) + \mathcal{A}_{ij}^E T_j^t + (\mathcal{K1}_{ij}^E + \mathcal{K2}_{ij}^E) T_j^t - \mathcal{F}_i^E - \mathcal{Q}_i^E = 0 \quad (3.8)$$

$i, j : 1 \rightarrow \text{NbLoc}$

where the volumetric contributions are detailed as follows:

$$\text{transient term: } \mathcal{M}_{ij}^E = \int_{\Omega_E} \frac{1}{\Delta t} \mathcal{P}_i \mathcal{P}_j \, dV \quad (3.9)$$

$$\text{advection term: } \mathcal{A}_{ij}^E = \int_{\Omega_E} \langle \rho \rangle^l C_p^l \mathcal{P}_i \langle \vec{v}^l \rangle \cdot \vec{\nabla} \mathcal{P}_j \, dV \quad (3.10)$$

$$\text{diffusion term: } \mathcal{K1}_{ij}^E = \int_{\Omega_E} \langle \kappa \rangle \vec{\nabla} \mathcal{P}_i \vec{\nabla} \mathcal{P}_j \, dV \quad (3.11)$$

$$\text{source term: } \mathcal{Q}_i^E = \int_{\Omega_E} \mathcal{P}_i \langle \dot{Q}_V \rangle \, dV \quad (3.12)$$

while the surface boundary contributions are given by:

$$\text{boundary condition term 1: } \mathcal{K}2_{ij}^E = \int_{\partial\Omega_E} h_{\text{ext}} \mathcal{P}_i \mathcal{P}_j \, dS \quad (3.13)$$

$$\text{boundary condition term 2: } \mathcal{F}_i^E = \int_{\partial\Omega_E} h_{\text{ext}} T_{\text{ext}} \mathcal{P}_i \, dS \quad (3.14)$$

$$(3.15)$$

The surface integrals  $\mathcal{K}2_{ij}^E$  and  $\mathcal{F}_i^E$  are related to a Fourier-type boundary condition, with  $h_{\text{ext}}$  as a coefficient of heat exchange and  $T_{\text{ext}}$  as the external temperature far from the boundary. The energy conservation principle is satisfied when the sum of the residual contributions coming from all the mesh elements is zero. In other words, the following global residual defined by the assembly of these contributions, should be minimized:

$$(R_i)^t = \mathcal{M}_{ij} \left( H_j^t - H_j^{t-\Delta t} \right) + \mathcal{A}_{ij} T_j^t + (\mathcal{K}1_{ij} + \mathcal{K}2_{ij}) T_j^t - \mathcal{F}_i - \mathcal{Q}_i = 0 \quad (3.16)$$

$$i, j : 1 \rightarrow \text{NbGlob}$$

where the global tensors  $\mathcal{M}_{ij}$ ,  $\mathcal{A}_{ij}$ ,  $\mathcal{K}1_{ij}$ ,  $\mathcal{K}2_{ij}$ ,  $\mathcal{F}_i$  and  $\mathcal{Q}_i$  contain respectively, after an assembly step, the contributions of the local matrices  $\mathcal{M}_{ij}^E$ ,  $\mathcal{A}_{ij}^E$ ,  $\mathcal{K}1_{ij}^E$ ,  $\mathcal{K}2_{ij}^E$ ,  $\mathcal{F}_i^E$  and  $\mathcal{Q}_i^E$  from each discretised element in the domain  $\Omega$ . Accordingly, the indices  $i$  and  $j$  refer to global node numbers, where the total number of nodes is denoted by "NbGlob".

It is clear that the global residual inherits the dependence between volumetric enthalpy and temperature. This is shown in [eq. \(3.16\)](#) where the average volume enthalpy is a function of the temperature. It infers that this residual is a non-linear function; therefore minimizing it requires an iterative non-linear algorithm.

Our choice settles on the Newton-Raphson method, known for its quadratic convergence speed. A solidification problem can induce severe non-linearities from the release of the latent heat (which itself is temperature and composition dependent) and the variations of the average thermophysical properties of the alloy with respect to temperature, phase fraction and average composition. This algorithm could thus treat such variations. Considering the link between the properties and temperature, [eq. \(3.16\)](#) may be solved either for the average volumetric enthalpy or for the temperature as the nodal unknown, hence both formulations are presented hereafter.

### 3.3.1 Enthalpy-based approach

The residual is re-written using a Taylor series expansion to the first order for a non-linear iteration ( $\nu$ ) :

$$(R_i)^{(\nu+1)} = (R_i)^{(\nu)} + \left( \frac{dR}{dH} \right)_{ij}^{(\nu)} \Delta H_j^{(\nu)} + \mathcal{O}(H_j^2) \quad (3.17)$$

Neglecting the second order terms, the suggested correction at each iteration in view of cancelling the residual and giving the new value  $H_j^{(\nu)}$ , is given by the linear system in eq. (3.18) relative to what we call a *Hsolver*:

$$\left( \frac{dR}{dH} \right)_{ij}^{(\nu)} (H_j^{(\nu+1)} - H_j^{(\nu)}) = -R_i^{(\nu)} \quad (3.18)$$

where  $\frac{dR}{dH}$  is a global tangent matrix yielding the variations of the residual with respect to the volumetric enthalpy in the previous iteration,  $H_j^{(\nu)}$ . The detailed flow chart for the *Hsolver* is given in fig. 3.3. If eq. (3.8) is considered, then the contribution of an element  $\Omega_E$  writes:

$$\left( \frac{dR^E}{dH} \right)_{ij}^{(\nu)} = \underbrace{\mathcal{M}_{ij}^E + \mathcal{A}_{ij}^E \left( \frac{dT}{dH} \right)_j^{(\nu)}}_{\text{no sum on } j} + \underbrace{(\mathcal{K}1_{ij}^E + \mathcal{K}2_{ij}^E) \left( \frac{dT}{dH} \right)_j^{(\nu)}}_{\text{no sum on } j} \quad (3.19)$$

Equation (3.19) is the core of the enthalpy-based solver. The resolution of eq. (3.18) then yields a new estimate of the vector of nodal volumetric enthalpies  $H^{(\nu+1)}$ , which are the only unknowns to be solved for. Once determined at iteration ( $\nu$ ), convergence tests are performed.

### 3.3.2 Temperature-based approach

Similarly to the *Hsolver*, the local residual is recast for a nonlinear iteration ( $\nu$ ), leading this time to an iterative temperature correction:

$$\left( \frac{dR}{dT} \right)_{ij}^{(\nu)} (T_j^{(\nu+1)} - T_j^{(\nu)}) = -R_i^{(\nu)} \quad (3.20)$$

where  $\frac{dR}{dT}$  is a global tangent matrix yielding the variations of the residual with respect to temperature  $T_j^{(\nu)}$  at the previous iteration. This solver will be referred to as *Tsolver*. The corresponding flow chart is given in fig. 3.4. The contribution of an element  $\Omega_E$

to this tangent matrix is evaluated as:

$$\left( \frac{dR^E}{dT} \right)_{ij}^{(\nu)} = \underbrace{\mathcal{M}_{ij}^E \left( \frac{dH}{dT} \right)_j^{(\nu)}}_{\text{no sum on } j} + \mathcal{A}_{ij}^E + (\mathcal{K}1_{ij}^E + \mathcal{K}2_{ij}^E) \quad (3.21)$$

In contrast to the previous solver, eq. (3.21) is the core of the temperature-based solver. The resolution of eq. (3.20) then yields a new estimate of the vector of nodal temperatures  $T^{(\nu+1)}$ , which are the only unknowns to be solved for. Once updated for iteration  $(\nu)$ , convergence tests are performed.

### 3.3.3 Convergence

The previous two sections described the iterative resolution of the same discretised energy conservation by both *Tsolver* and *Hsolver*. However, in eqs. (3.19) and (3.21), an important term emerges from the tangent matrix evaluation describing the variations between enthalpy and temperature:  $\frac{dT}{dH}$  and  $\frac{dH}{dT}$ .

This term invokes the previously mentioned temperature-enthalpy tabulations which depend on the alloy composition. Consequently,  $\frac{dT}{dH}$  (respectively  $\frac{dH}{dT}$ ) has a great influence on the convergence of the *Hsolver* (respectively the *Tsolver*). When eq. (3.18) or eq. (3.20) is solved at iteration  $(\nu)$ , this term is written using a finite difference:

$$\mathbf{Hsolver} \quad \left( \frac{dT}{dH} \right)_j^{(\nu+1)} = \frac{T_j^{(\nu+1)} - T_j^{(\nu)}}{\langle \rho h \rangle_j^{(\nu+1)} - \langle \rho h \rangle_j^{(\nu)}} \quad (3.22)$$

$$\mathbf{Tsolver} \quad \left( \frac{dH}{dT} \right)_j^{(\nu+1)} = \frac{\langle \rho h \rangle_j^{(\nu+1)} - \langle \rho h \rangle_j^{(\nu)}}{T_j^{(\nu+1)} - T_j^{(\nu)}} \quad (3.23)$$

For the *Tsolver*, the enthalpy  $\langle \rho h \rangle_j^{(\nu)}$  is needed to evaluate eq. (3.23). In contrast, the *Hsolver* requires the value of  $T_j^{(\nu)}$  to evaluate the corresponding eq. (3.22). In both cases, the unknown is determined by the tabulations. The indices next to the mentioned unknowns indicate that this relation is used for each iteration  $(\nu)$  at each mesh node  $j$ , hence affecting the global resolution time between the two solvers. The *Hsolver* needs a  $H2T$  to evaluate  $\frac{dT}{dH}$ , whereas the *Tsolver* needs a  $T2H$  to evaluate  $\frac{dH}{dT}$ . It can be seen that *Tsolver* uses solely  $T2H$  procedure (flowchart in fig. 3.1) and the thermodynamic tabulations to determine the volumetric enthalpy, hence the term  $\frac{dH}{dT}$ . On the other hand, *Hsolver* repeats the same procedure a finite number of times in order to determine a temperature output through  $H2T$  (flowchart in fig. 3.2) and use it to compute  $\frac{dT}{dH}$ . This algorithmic difference leverages the *Tsolver* in terms of computa-

tion time providing the same numerical accuracy while conserving the total system energy.

Convergence tests are necessary at the end of each iteration of the energy solver to determine the convergence status of the algorithm. In the context of the *Tsolver* for instance, the residual is re-evaluated with the newly determined temperature  $T_j^{(\nu+1)}$  and enthalpy  $H_j^{(\nu+1)}$  so [eq. \(3.16\)](#) rewrites:

$$(R_i)^{(\nu+1)} = \mathcal{M}_{ij} \left( H_j^{(\nu+1)} - H_j^{t-\Delta t} \right) + \mathcal{A}_{ij} T_j^{(\nu+1)} + (\mathcal{K}1_{ij} + \mathcal{K}2_{ij}) T_j^{(\nu+1)} - \mathcal{F}_i - \mathcal{Q}_i$$

$$i, j : 1 \rightarrow \text{NbGlob}$$
(3.24)

The norm of the current residual,  $\|R^{(\nu+1)}\|$ , is compared to a fixed small value  $\varepsilon_R \approx [10^{-5}; 10^{-4}]$ . The resulting temperature variation,  $|T_j^{(\nu)} - T_j^{(\nu-1)}|$ , should also respond to similar criterion between two consecutive iterations. For that purpose, we compare it to another fixed value  $\varepsilon_T \approx [10^{-3}; 10^{-2}]$ . Convergence is ultimately achieved when the following criteria are simultaneously met:

$$\begin{cases} \|R^{(\nu+1)}\| < \varepsilon_R \\ \text{Max}_{j:1 \rightarrow \text{NbGlob}} |T_j^{(\nu+1)} - T_j^{(\nu)}| < \varepsilon_T \end{cases} \quad (3.25)$$

A comparison of both solver formulations is done in the hereafter test cases section.

### 3.4 Validation

The two solvers are tested in a purely diffusive case for a one-dimensional solidification configuration. Predictions with a 1D front tracking model [[Gandin 2000](#)] is used as a benchmark. It provides solutions for the temperature and solid fraction during directional solidification of a 10 cm long ingot. Its nominal composition,  $w_0$ , is Al-7 wt.% Si. The melt having a uniform initial temperature,  $T_0$ , is cooled with a heat exchange coefficient,  $h_{\text{ext}}$ , with a fixed external temperature,  $T_{\text{ext}}$  (assuming a Fourier boundary condition) from one side, the other side being adiabatic. The initial conditions, boundary conditions and alloy properties are all listed in [table 3.2](#).

For this simple test case, we use linear temperature dependence of the intrinsic phase enthalpies, that is  $\langle \rho h \rangle^s = \rho C_p T$  and  $\langle \rho h \rangle^l = \rho(C_p T + L)$ , where  $\rho$  is the alloy density,  $C_p$  is the heat capacity per unit mass and  $L$  is the latent heat per unit mass. Values for  $\rho$ ,  $C_p$  and  $L$ , as well as for the thermal conductivities,  $\kappa = \langle \kappa \rangle^l = \langle \kappa \rangle^s$ , are taken constant.

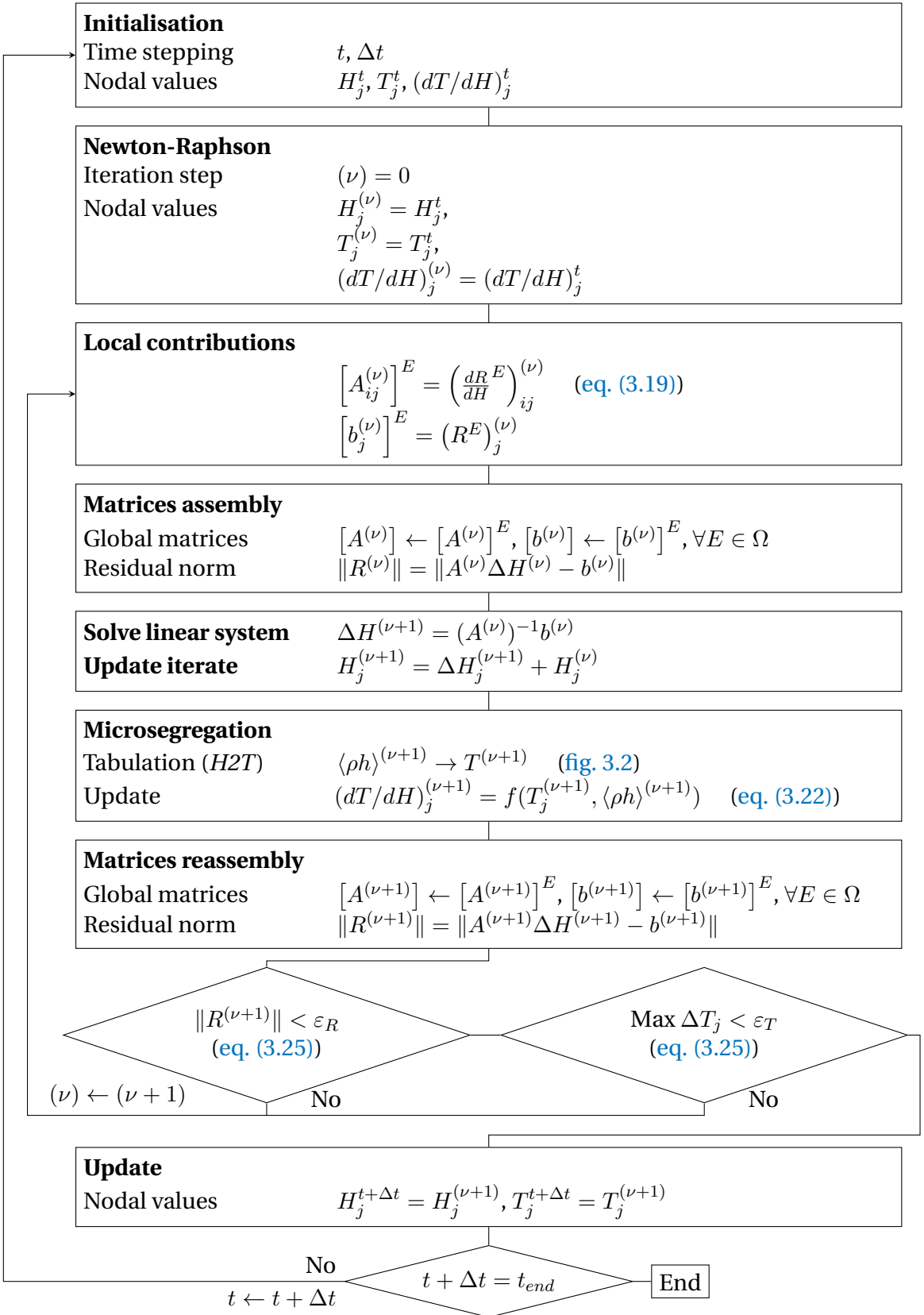
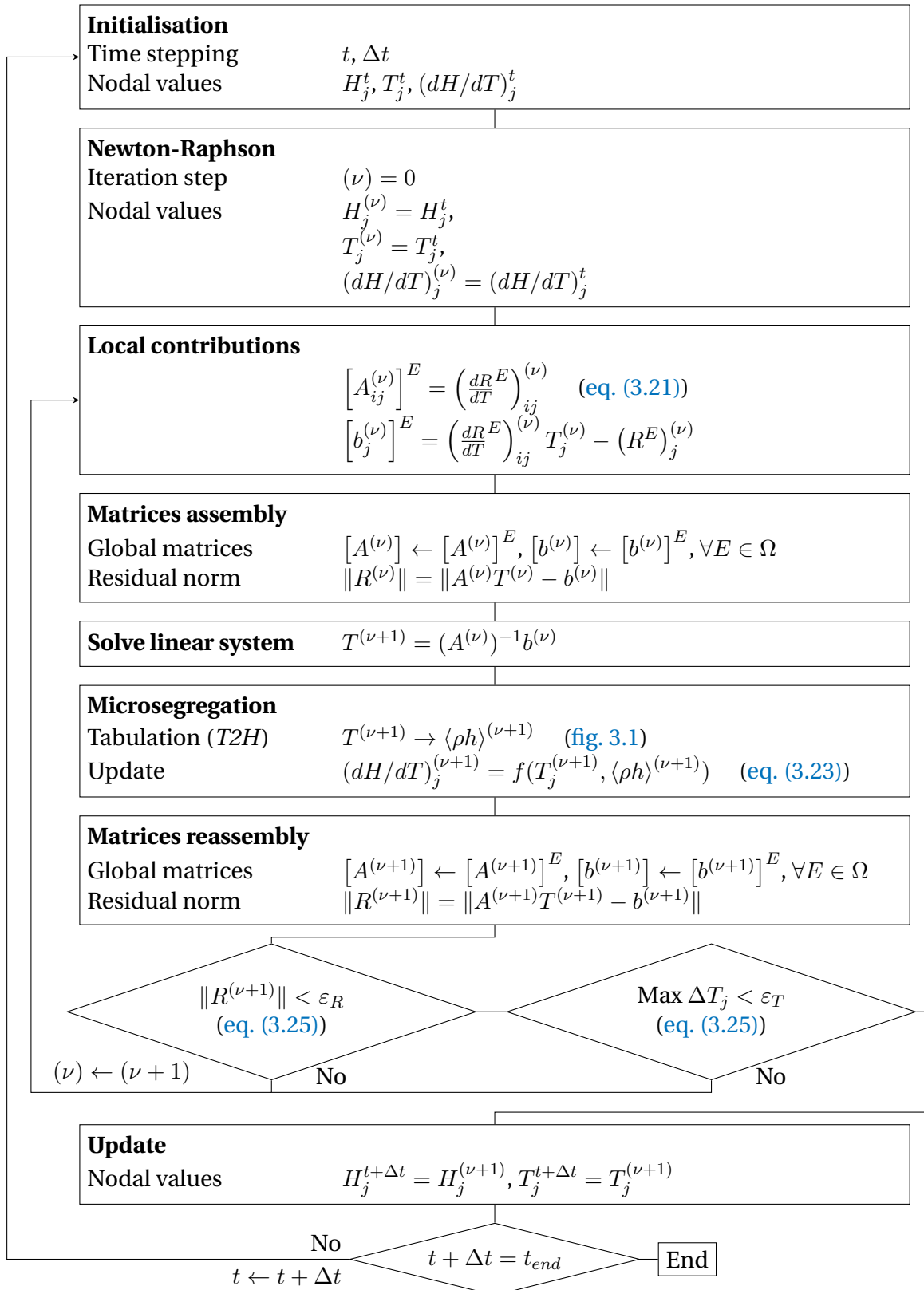


Fig. 3.3 – Resolution algorithm of the enthalpy-based solver.

### Chapter 3. Energy balance with thermodynamic tabulations



**Fig. 3.4 – Resolution algorithm of the temperature-based solver.**

### 3.5. Application: multicomponent alloy solidification

---

A Gulliver-Scheil approximation is used to compute a single relationship between temperature and volume solid fraction,  $g^s$ , in the absence of macrosegregation. This is done assuming a linear binary phase diagram and thus requires using the properties listed in [table 3.2](#), i.e. the segregation coefficient,  $k$ , the liquidus slope,  $m_L$ , the liquidus temperature,  $T_L$ , and the eutectic temperature,  $T_E$ . [Figure 3.5](#) show the comparison with the *Hsolver* and *Tsolver*. The cooling curves and liquid fraction results are found superimposed to the front tracking solution, thus giving validation of the implementation as well as the iterative schemes presented above to solve the energy conservation

**Table 3.2** – Parameters for the pure diffusion test case with an Al-7 wt.% Si alloy presented in [fig. 3.5](#)

Parameter	Symbol	Value	Unit
Nominal composition	$w_0$	7	wt.%
Liquidus temperature	$T_L$	618	°C
Eutectic temperature	$T_E$	577	°C
Segregation coefficient	$k$	0.13	–
Liquidus slope	$m_L$	-6.5	K wt.% <sup>-1</sup>
Density	$\rho$	2600	kg m <sup>-3</sup>
Liquid heat capacity	$C_p$	1000	J kg <sup>-1</sup> K <sup>-1</sup>
Enthalpy of fusion	$L$	365 384	J kg <sup>-1</sup>
Thermal conductivity	$\kappa$	70	W m <sup>-1</sup> K <sup>-1</sup>
Heat transfer coefficient	$h_{\text{ext}}$	500	W m <sup>-2</sup> K <sup>-1</sup>
External temperature	$T_{\text{ext}}$	100	°C
Initial temperature	$T_0$	800	°C
Ingot length		0.1	m
FE mesh size		$10^{-3}$	m
Time step	$\Delta t$	0.1	s
Convergence criterion (residual)	$\varepsilon_R$	$10^{-6}$	–
Convergence criterion (temperature)	$\varepsilon_T$	$10^{-2}$	K

## 3.5 Application: multicomponent alloy solidification

We have shown that the efficiency of the temperature-based resolution resides in its performance when combined with thermodynamic tabulations. A multicomponent alloy consists of at least two solute elements, and therefore the tabulation size increases, hence the number of search operations also increases. To demonstrate the

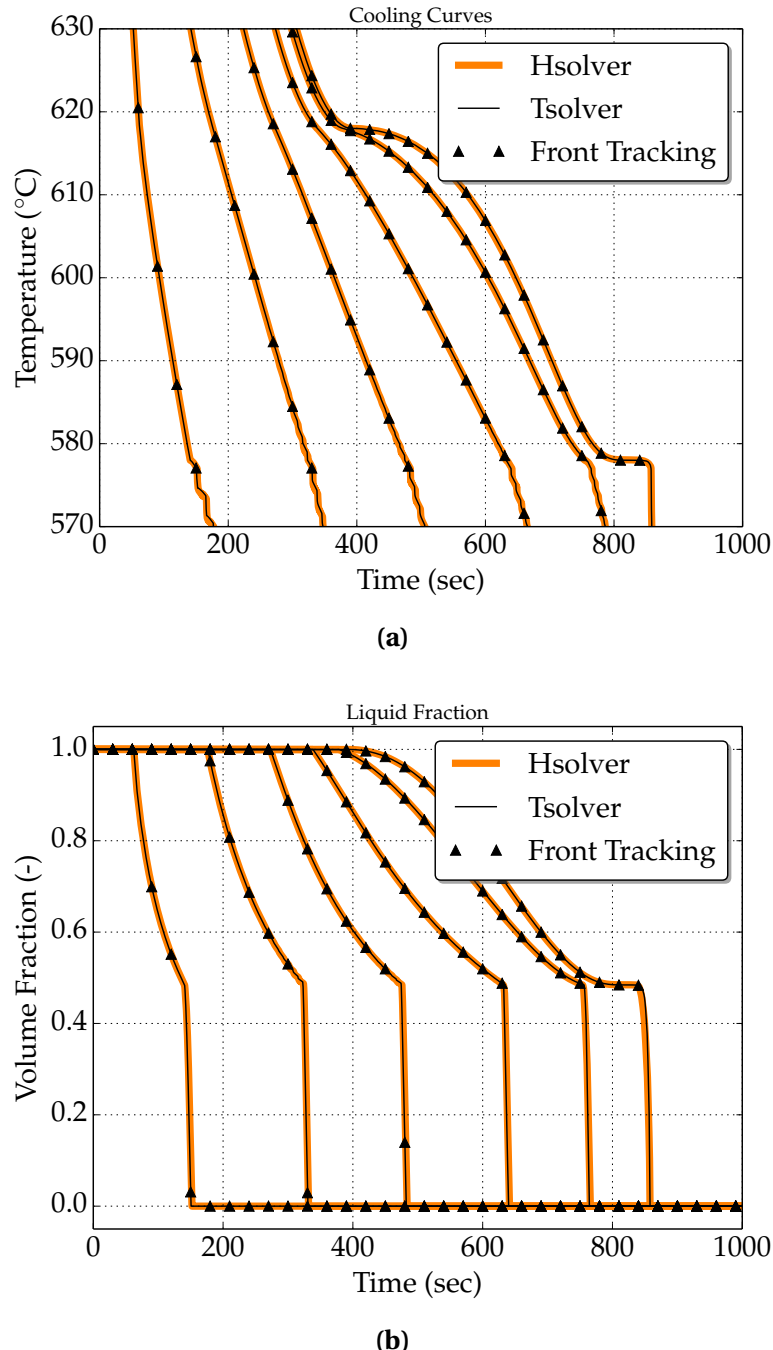


**Fig. 3.5** – Computed unidirectional heat diffusion during solidification of an Al-7 wt.% Si alloy using (orange) the enthalpy method and (black) the temperature method, comparison being made for (a) cooling curves and (b) the liquid fraction history. Each curve corresponds to a position along the sample, from 0 cm (cooling side) to 10 cm (insulated side), with 2 cm spacing between the positions. The reference solution by the Front Tracking method (values in shown by the triangular markers).

speed-up ability of the temperature-based approach while predicting all phase transformations during macrosegregation caused solely by mass diffusion, we consider the solidification of a ternary alloy, Fe-2 wt.% C-30 wt.% Cr. In order to neglect fluid flow resolution, we assume that solidification in this case is so slow that no forces are generated inside the melt, while additionally all buoyancy forces are also neglected, so no momentum conservation is solved in this section.

As illustrated in [fig. 3.6a](#), the alloy domain has a cylinder shape close to 3-inch height  $\times$  1-inch diameter. Exact values are reported in [table 3.3](#) with all material properties, initial and boundary conditions, as well as numerical parameters for the simulations. The melt steel is initially at 1395 °C. The temperature of the bottom surface is imposed with a constant decreasing rate of 0.1 K s<sup>-1</sup> starting with 1380 °C as shown in [fig. 3.6b](#), i.e. 40 °C higher than the nominal liquidus temperature as shown in [fig. 3.7](#). The other surfaces are kept adiabatic.

The cylinder is held in a vertical position parallel to the gravity vector, the latter pointing downwards. [fig. 3.7](#) also provides the transformation path of the alloy at nominal composition, i.e. assuming no macrosegregation and full thermodynamic equilibrium as computed with ThermoCalc and the TCFE6 database [[TCFE6 2010; Andersson et al. 2002](#)]. A total of 5 phases need to be handled, the characteristic temperature for their formation being reported in [fig. 3.6b](#).

#### 3.5.1 Tabulations

Full thermodynamic equilibrium is considered in the present case. Due to macrosegregation, the average composition is expected to continuously vary in time and space during casting. Transformation paths are thus determined a priori for a set of average compositions around the nominal value. Hence, carbon content varies in the interval [1.8 wt.%, 2.2 wt.%] while chromium content variation is in the interval [27 wt.%, 33 wt.%]. The offset of  $\pm 10\%$  with respect to the nominal composition value allows tabulating relatively small composition steps to ensure a fairly accurate mapping when compared to the corresponding ternary phase diagram.

The average composition step is 0.04 wt.% for carbon and 0.6 wt.% for chromium, thus representing 2% intervals with respect to the nominal composition. The temperature varies in the interval [100 °C, 1600 °C] by 5 °C steps. For each triplet (carbon content in wt.% C,  $w_{C0}$ , chromium content in wt.% Cr,  $w_{Cr0}$ , temperature in K) corresponds a phase fraction  $g^\phi$  and a pair of intrinsic phase composition ( $\langle w_C \rangle^\phi, \langle w_{Cr} \rangle^\phi$ ). For the 5 phases listed in [fig. 3.7](#) (LIQ≡liquid, BCC≡ferrite, FCC≡austenite, M<sub>7</sub>C<sub>3</sub>≡carbide, CEM≡cementite), the enthalpy  $\langle h \rangle^\phi$  and density  $\langle \rho \rangle^\phi$ , are tabulated as functions of temperature and phase intrinsic composition. If this latter input lies between two tab-

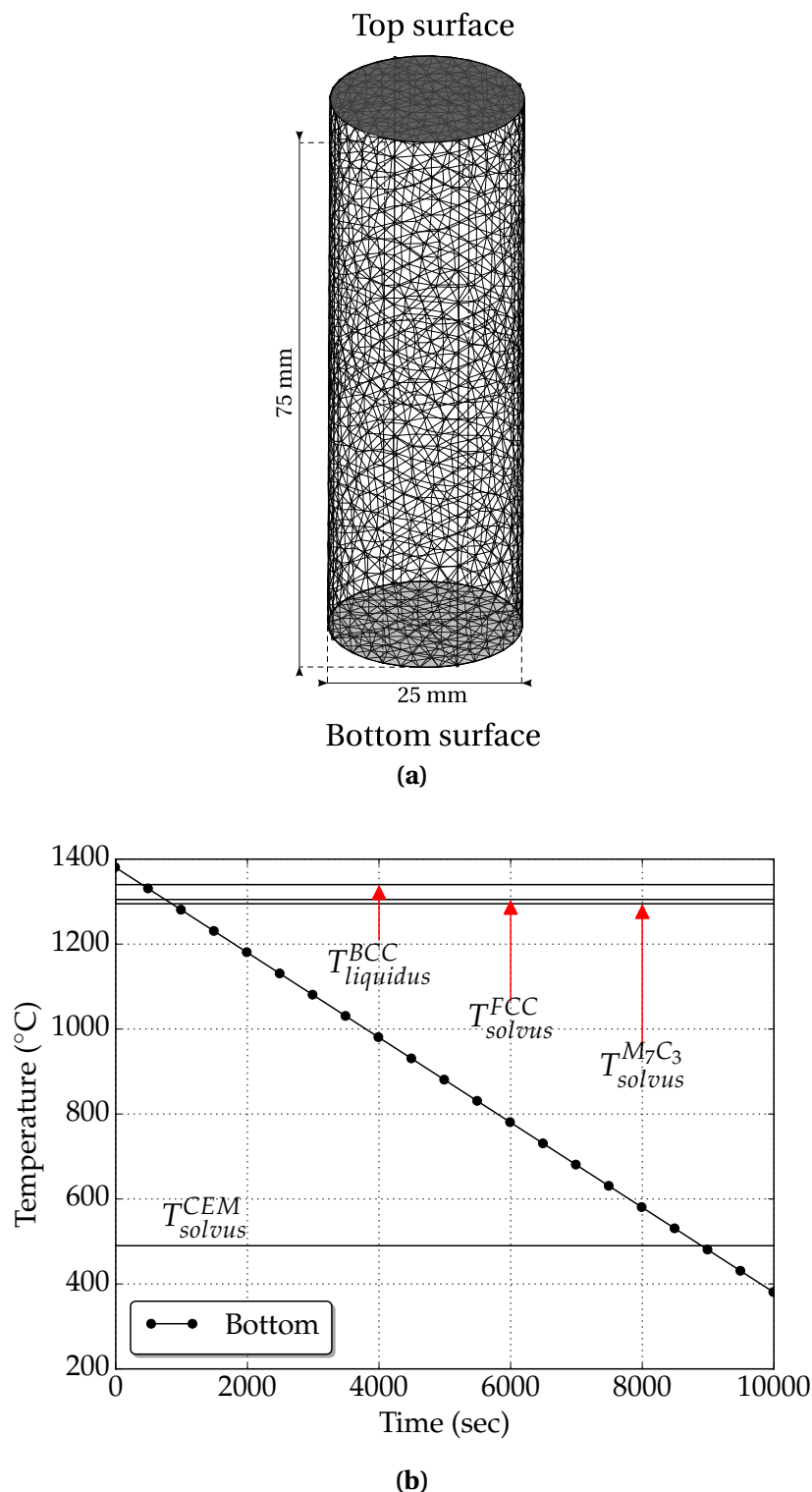


**Fig. 3.6** – Configurations for upward directional casting of (a) a 1-inch diameter × 3-inches height cylindrical domain for which (b) temperature-time conditions are imposed at its bottom surface.

### 3.5. Application: multicomponent alloy solidification

ulated values, a linear interpolation is performed to determine the output, i.e. phase enthalpy and density. With the advancement of solidification, the liquid is enriched or depleted with solute by macrosegregation, which enables new solidification paths. It means that the primary solidifying phase is not necessarily the same as when considering the nominal composition. For this reason, the tabulation approach is interesting inasmuch as it provides phase transformation paths and values of phase properties that are compatible with the system's actual composition.

[Figure 3.8](#) summarises the tabulated thermodynamic data for two sets of average composition for the considered ternary system. Note that in the present test case, phase densities are taken constant ( $\langle \rho \rangle^s = \langle \rho \rangle^l = 6725 \text{ kg m}^{-3}$ ). Therefore they are not tabulated. With this assumption, no shrinkage occurs upon phase change.

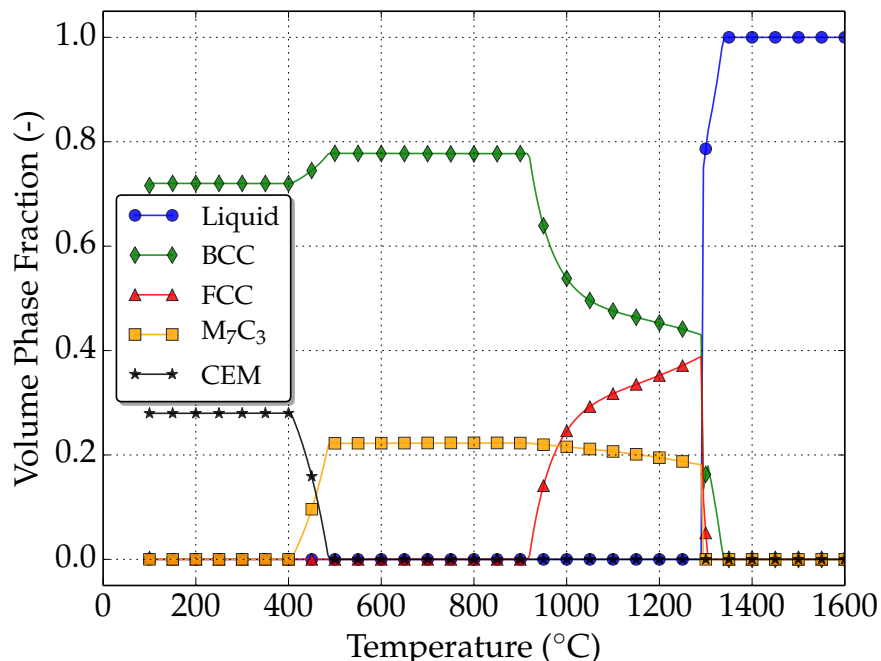


**Fig. 3.7 –** Thermodynamic mapping [TCFE6 2010; Andersson et al. 2002] of the transformation path for the Fe-2 wt.% C-30 wt.% Cr at nominal composition.

#### 3.5.2 Discussion

A first case is considered without macrosegregation, that is, all mechanical driving forces are bypassed, leading to a static melt. This is achieved by nullifying the thermal and solutal expansion coefficients, which is equivalent to a constant density in space and time, i.e. no Boussinesq force is considered. This way, the average composition may only vary due to diffusion in the liquid phase.

### Chapter 3. Energy balance with thermodynamic tabulations

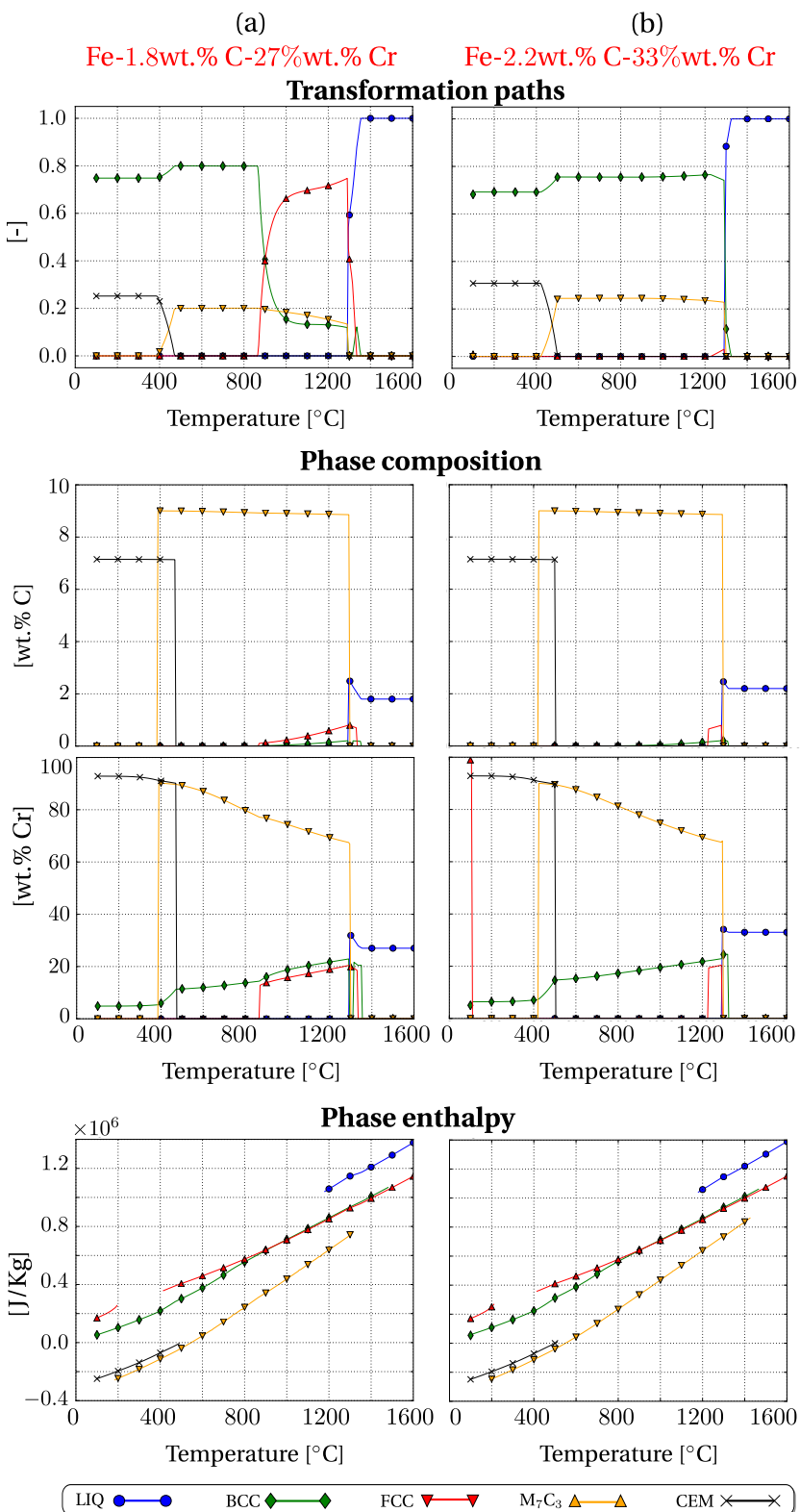


**Fig. 3.8** – Tabulated thermodynamic data for the ternary system Fe-Cr alloy with software Thermo-Calc [Andersson et al. 2002] with database TCFE6 [TCFE6 2010]. The two columns represent two values of nominal average composition, for a) low carbon and chromium content and b) high carbon and chromium content. The effect of their variation on transformation paths, phase compositions and phase enthalpies is shown in the corresponding graphs.

### **3.5. Application: multicomponent alloy solidification**

---

Diffusion is significantly small in the present case and can be neglected too. The composition distribution thus maintains a homogeneous aspect throughout the sample during the entire cooling sequence. The phase transformations then are necessarily expected to follow the unique path shown in [fig. 3.7](#). After 407 s of cooling, the liquidus isotherm enters the bottom surface of the geometry and starts its upward propagation, marking the solidification onset.

[Figure 3.9](#) presents the simulation results at 3 successive times for the distribution of the solute species and the temperature, as well as for the fraction of phases listed in [fig. 3.7](#). At 600 s, a fully liquid region is still largely present while the mushy zone is made of liquid plus the primary solid phase (ferrite). At 10 560 s, the sample is full solid, with fractions of ferrite and cementite that corresponds to the values read in [fig. 3.7](#) at low temperature. At the selected intermediate time, the presence of 4 phases is found. The solid region at the bottom of the cylinder is made of ferrite, austenite plus carbide, the temperature being still too high to permit the cementite to form. The mushy zone above the solid region is characterized by the presence of 3 phases due to a peritectic reaction taking place that progressively transform ferrite into austenite in the presence of liquid.

It can be noticed that the phase fraction isovales in [fig. 3.9](#) (at 600 s) are horizontal, owing this to two factors: the first is the temperature field, which varies unidirectionally from bottom to top, controlled by thermal diffusion, while the second is the uniform average composition throughout the sample due to the absence of convection. In fact both factors are consequences of the flow absence, which would transport heat and solute by advection, thus inevitably changing the phase distribution. The succeeding phase change is a solid-state transformation where  $\alpha$ -ferrite and the carbide  $M_7C_3$  react to form cementite at 490 °C at nominal composition, as shown in [fig. 3.6b](#). The reaction is relatively slow, ending with 28% of cementite and 72% of  $\alpha$ -ferrite.

### Chapter 3. Energy balance with thermodynamic tabulations

---

**Table 3.3** – Solidification parameters for the Fe-2 wt.% C-30 wt.% Cr alloy.

Parameter	Symbol	Value	Unit
Nominal composition	$w_{C0}$	2	wt.%
	$w_{Cr0}$	30	wt.%
Characteristic temperatures	$T_{\text{bottom}}$	<a href="#">fig. 3.6b</a>	°C
Phase fraction	$g^\phi$	Tabulations <a href="#">fig. 3.8</a>	–
Phase enthalpy	$\langle h \rangle^\phi$	Tabulations <a href="#">fig. 3.8</a>	–
Phase composition	$\langle w_C \rangle^\phi$	Tabulations <a href="#">fig. 3.8</a>	wt.%
Phase composition	$\langle w_{Cr} \rangle^\phi$	Tabulations <a href="#">fig. 3.8</a>	wt.%
Diffusion coefficients	$\langle D_C \rangle^l$	$15 \times 10^{-10}$	$\text{m}^2 \text{s}^{-1}$
	$\langle D_{Cr} \rangle^l$	$15 \times 10^{-10}$	$\text{m}^2 \text{s}^{-1}$
Dynamic viscosity	$\mu^l$	$2 \times 10^{-3}$	Pa s
Thermal expansion coefficient	$\beta_T$	$8.96 \times 10^{-5}$	$\text{K}^{-1}$
Solutal expansion coefficient	$\beta_{\langle w_C \rangle^l}$	$1.54 \times 10^{-3}$	$\text{wt.\%}^{-1}$
	$\beta_{\langle w_{Cr} \rangle^l}$	$1.72 \times 10^{-2}$	$\text{wt.\%}^{-1}$
Thermal conductivity in the solid	$\langle \kappa \rangle^s$	40	$\text{W m}^{-1} \text{K}^{-1}$
Thermal conductivity in the liquid	$\langle \kappa \rangle^l$	28	$\text{W m}^{-1} \text{K}^{-1}$
Dendrite arm spacing	$\lambda$	$60 \times 10^{-6}$	m
Density	$\rho_0^l$	6725	$\text{kg m}^{-3}$
Reference composition (carbon)	$\langle w_C \rangle_{\text{ref}}^l$	2	wt.%
Reference composition (chromium)	$\langle w_{Cr} \rangle_{\text{ref}}^l$	30	wt.%
Reference temperature	$\langle w_C \rangle_{\text{ref}}^l$	1377	°C
Initial temperature	$T_0$	1395	°C
Ingot diameter		$25 \times 10^{-3}$	m
Ingot length		$75 \times 10^{-3}$	m
FE mesh size		$10^{-3}$	m
Time step	$\Delta t$	0.1	s
Convergence criterion (residual)	$\varepsilon_R$	$10^{-6}$	–
Convergence criterion (temperature)	$\varepsilon_T$	$10^{-2}$	K

### 3.5. Application: multicomponent alloy solidification

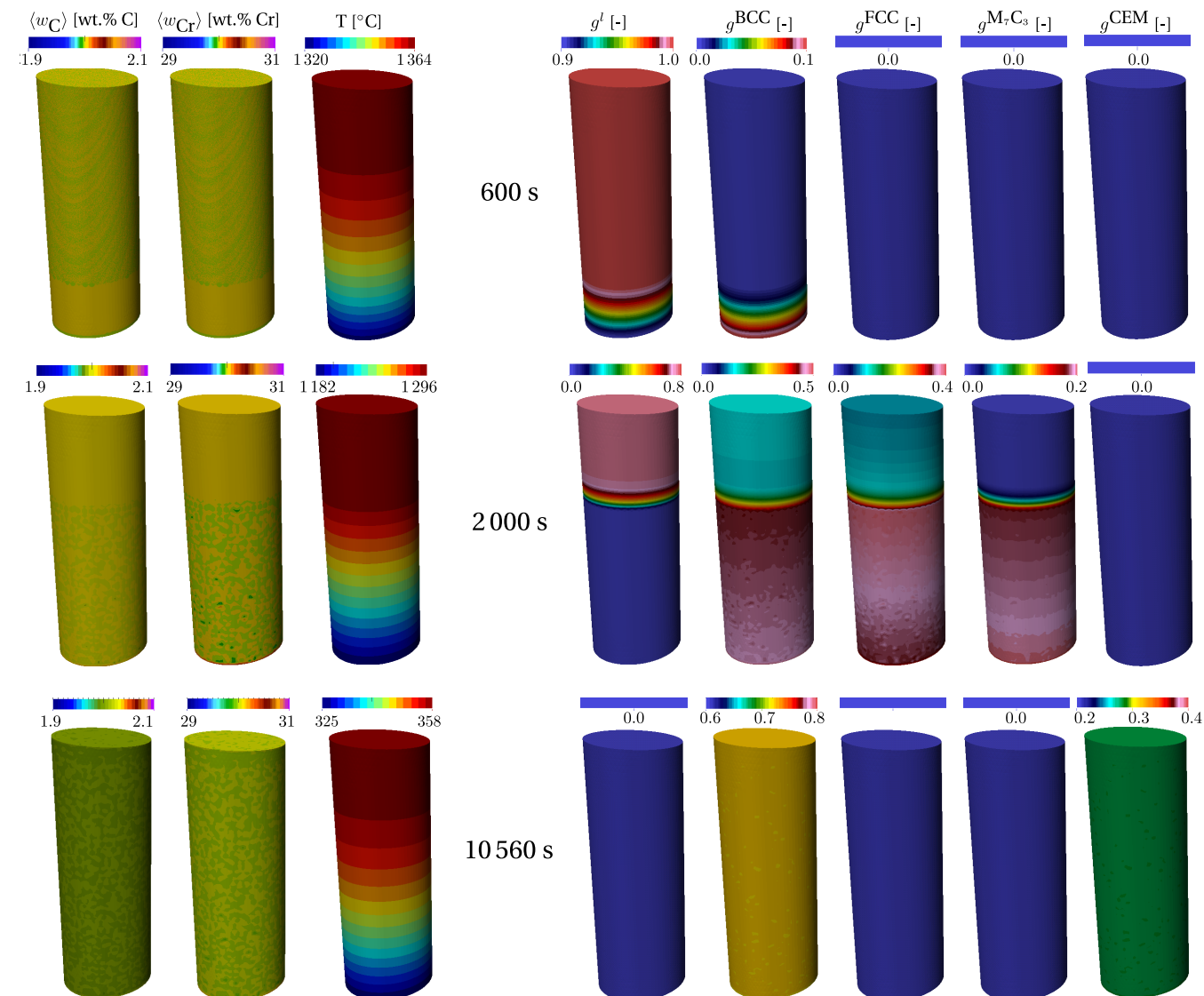


**Fig. 3.9 –** Upward solidification of a cylinder rod with a static liquid at 3 stages in a Fe-2 wt.% C-30 wt.% Cr. The left columns show the average composition and temperature distribution, while the right columns show the phase fractions.

## Résumé chapitre 3

Ce chapitre reprend les détails du solveur pour la conservation d'énergie avec changement de phase utilisé au CEMEF. Celui-ci est basé sur une méthode enthalpique, dénommée *Hsolver*, dont la variable principale est l'enthalpie moyenne volumique du système,  $\langle \rho h \rangle$ . Ce solveur est aussi compatible avec des données tabulées provenant de bases de données thermodynamiques, fournissant des valeurs précises pour chaque phase  $\phi$  présente au moment de la transformation: fraction  $g^\phi$ , composition intrinsèque  $\langle w_i \rangle^\phi$ , enthalpie massique  $\langle h \rangle^\phi$  et densité  $\langle \rho \rangle^\phi$ . Avec ces données, l'équation de conservation de l'énergie est résolue dans son état nonlinéaire provenant de la dépendance de  $\rho h$  par rapport aux propriétés citées précédemment, sachant que celles-ci varient aussi en fonction de la composition moyenne du volume élémentaire représentatif.

Cependant, la résolution *Hsolver* nécessite une lourde recherche itérative à chaque pas de temps, consistant à convertir  $\langle \rho h \rangle$  en température  $T$  pour évaluer le résidu du système nonlinéaire. Cette conversion est dénommée *H2T* et elle est compliquée du fait que les bases thermodynamiques fournissent la température comme donnée d'entrée, ce qui nous oblige de faire la recherche inverse itérative.

Dans ce chapitre, on propose de remplacer la conversion *H2T* par une autre, *T2H*. Comme son nom l'indique, on part de l'idée que la température soit la variable principale du système et on devrait alors trouver l'enthalpie moyenne volumique à chaque pas de temps. Avec ce changement, on propose donc une nouvelle formulation éléments finis, *Tsolver*, mettant en évidence les principales différences algorithmiques des deux résolutions.

Nous validons la formulation *Tsolver* dans un cas purement diffusif et comparé à des calculs faits avec la méthode *Hsolver*, ainsi qu'une comparaison avec une solution numérique obtenue par une méthode de suivi de front [Gandin 2000]. Enfin, nous montrons une application de solidification dirigée d'un système ternaire, Fe-0.2 wt.% C-30 wt.% Cr, en régime diffusif.

## Chapter 4

# Macrosegregation with liquid metal motion

## Contents

---

<b>4.1</b>	<b>Introduction</b>	73
<b>4.2</b>	<b>Formulation stability</b>	73
4.2.1	Stable mixed finite elements	73
4.2.2	Variational multiscale (VMS)	74
<b>4.3</b>	<b>Navier-Stokes solver</b>	75
4.3.1	Strong and weak formulations	75
4.3.2	Stabilisation parameters	79
4.3.3	Implementation	80
<b>4.4</b>	<b>Application to multicomponent alloys</b>	81
4.4.1	<i>Tsolver</i> validation with fluid flow	81
4.4.2	Results	84
<b>4.5</b>	<b>Macroscopic prediction of channel segregates</b>	87
4.5.1	Introduction	87
4.5.2	Experimental work	89
4.5.3	Macroscopic scale simulations	89
<b>4.6</b>	<b>Meso-Macro prediction of channel segregates</b>	97
4.6.1	Numerical method	97
4.6.2	Configuration	98
4.6.3	Effect of vertical temperature gradient	103
4.6.4	Effect of cooling rate	105
4.6.5	Effect of lateral temperature gradient	107

## **Chapter 4. Macrosegregation with liquid metal motion**

---

4.6.6 Mono-grain freckles . . . . .	108
-------------------------------------	-----

---

## 4.1 Introduction

Fluid flow is an important part, if not the most important, in understanding the evolution of a system undergoing phase change and chemical segregation. It is attributed to the convective transport in fluids where the variations time scale is much smaller than the remaining physics that are characterised by smoother variations. To understand how fluid motion contributes to the heat and mass transfer, we have swiftly presented the momentum conservation equation in a solidifying liquid, [eq. \(2.41\)](#). In this chapter, we will first give quick overview of the numerical treatment of this system of Navier-Stokes equations, then comment on some computational aspects such as the choice of a suitable time step and the conditions that impose minimum and maximum bounds on both time step and mesh size.

## 4.2 Formulation stability

A wide array of numerical methods can be used to solve systems like [eq. \(2.41\)](#). When speaking about Navier-Stokes equations, the choice can be narrowed to two famous approaches with some similarities: stable mixed finite element method and Variational MultiScale (VMS) method. When two finite element spaces are introduced (e.g. one for velocity and another for pressure), the essential *inf-sup* condition (also known as stability condition) determined by [Babuška \[1971\]](#) and [Brezzi \[1974\]](#) should be fulfilled. It states that the formulation is not well-posed if the both spaces have the same interpolation order. For instance, a P1/P1 element (i.e. P1 for velocity / P1 for pressure) cannot guarantee the stability of the Navier-Stokes solution since velocity and pressure are both linearly interpolated at the simplex vertices. However, the major difference between the previously mentioned formulations is the way in which the inf-sup condition is accounted for. Stable mixed finite elements are stable because they directly respond to the stability condition by enriching the velocity space, hence they fall under the category of Satisfying Babuška-Brezzi (SBB) methods. In contrast, methods like VMS belong to the Circumventing Babuška-Brezzi (CBB) category [[Barbosa and Hughes 1991](#)]. CBB methods rely on equal-order interpolations with additional stabilisation that circumvents the need to satisfy the stability condition. Further details about both formulation types are given in the next subsections.

### 4.2.1 Stable mixed finite elements

First introduced by [Arnold et al. \[1984\]](#), the MINI element is the key ingredient of this approach. This type of element introduces an additional degree of freedom for the

velocity field while keeping a linear interpolation for the pressure field, thus satisfying the Babuška-Brezzi condition with a richer velocity space. The additional degree, known as the *bubble* function, vanishes on the element's boundary. We may therefore speak of a P1+/P1 finite element in a velocity-pressure formulation. This stable formulation has been the de facto standard for solving fluid and solid mechanics for many years at CEMEF.

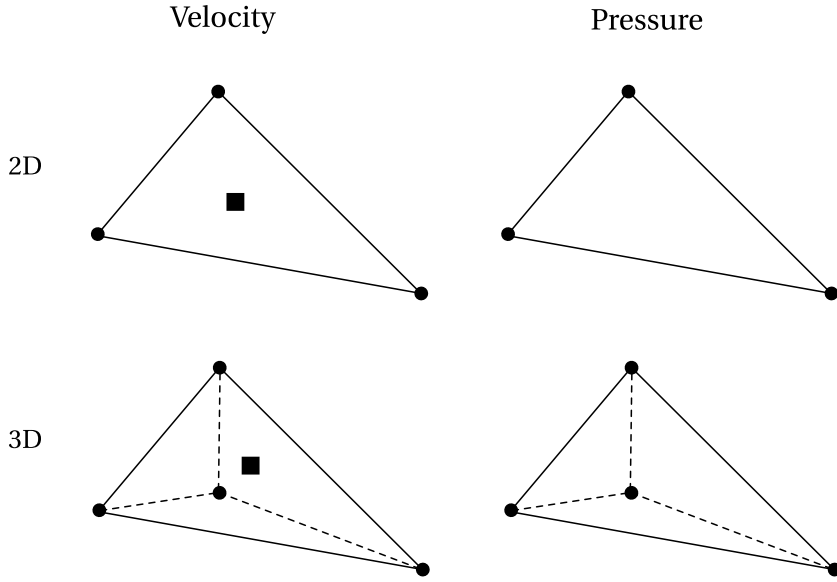


**Fig. 4.1** – Schematic of 2D and 3D stable P1+/P1 finite elements, respectively triangle and tetrahedron, with velocity and pressure fields interpolation order. The dots represent the nodes while the squares represent the bubbles.

#### 4.2.2 Variational multiscale (VMS)

As the name indicates, this approach considers two scales of phenomena: the coarse and fine scales. Applied to a velocity-pressure formulation, these fields are decomposed according to these scales as follows:

$$\langle \vec{v}^l \rangle = \langle \vec{v}^l \rangle_h + \tilde{\vec{v}}^l \quad (4.1)$$

$$p = p_h + \tilde{p} \quad (4.2)$$

where  $\langle \vec{v}^l \rangle_h$  and  $p_h$  are the coarse scale velocity and pressure discretised on the finite element mesh (hence the subscript  $h$ ), while the remaining terms represent the fine scale velocity and pressure that cannot be captured at the scale of the FE grid. Instead of defining a finer grid to model the effect of these terms, one can solve the fine scale equations obtained once [eqs. \(4.1\) and \(4.2\)](#) are injected in [eq. \(2.41\)](#) then use the

output in the coarse scale equations. Further technical details about the method and the equations are found in the PhD work of [Hachem \[2009\]](#).

The added value of the VMS method is the time gain that we get by incorporating the effect of the fine scale into the coarse scale physics without discretising on a finer grid, while maintaining the ability to predict localised fluid motion such as small vortices.

## 4.3 Navier-Stokes solver

In the present thesis, we chose to solve the fluid momentum conservation using a stabilised P1/P1 formulation with additional element-level integrals to add stability for convection-dominated terms, transient-dominated terms and pressure terms. The stabilisation techniques include the streamline upwind/Petrov-Galerkin (SUPG), pressure stabilising/Petrov-Galerkin (PSPG) and the least-squares on incompressibility constraint (LSIC) as a stabilisation framework introduced by [Tezduyar et al. \[1992\]](#). The global approach, more commonly known as SUPG-PSPG-LSIC, prevents the classical formulation instability coming from the linear equal-order interpolation functions.

It is important to note that the P1/P1 SUPG-PSPG-LSIC approach is slightly different than a VMS approach as the derivation of stabilising terms in the latter comes from a physical interpretation of two different length scales, a resolved coarse scale and an unresolved fine scale. The incorporation of the fine-scale equation within the coarse-scale one results in additional stabilising terms, while in the current approach these terms come from a mathematical analysis based on limiting cases of diffusion or advection. The final stabilising scheme is however very similar. The Navier-Stokes solver developed by [Hachem et al. \[2010\]](#) and [Rivaux \[2011\]](#) is a convenience choice to solve a stabilised Navier-Stokes system with Darcy terms.

### 4.3.1 Strong and weak formulations

The strong form of the fluid mechanics problem has been previously established in chapter 2 ([section 2.1.1](#)), where we obtained the following system of mass and liquid

## Chapter 4. Macrosegregation with liquid metal motion

---

momentum conservation equations:

$$\left\{ \begin{array}{l} \rho_0^l \left( \frac{\partial \langle \vec{v}^l \rangle}{\partial t} + \frac{1}{g^l} \vec{\nabla} \cdot (\langle \vec{v}^l \rangle \times \langle \vec{v}^l \rangle) \right) = \\ - g^l \vec{\nabla} p^l - \vec{\nabla} \cdot (2\mu^l \langle \vec{\varepsilon}^l \rangle) - g^l \mu^l \mathbb{K}^{-1} \langle \vec{v}^l \rangle + g^l \langle \rho \rangle^l \vec{g} \\ \nabla \cdot \langle \vec{v}^l \rangle = 0 \end{array} \right. \quad (4.3)$$

The strong solution consists of finding the pair  $(\langle \vec{v}^l \rangle, p^l)$  of the previous system, when the following essential (Dirichlet type) and natural (Neumann type) boundary conditions are applied :

$$\langle \vec{v}^l \rangle = \vec{v}_0 \text{ on } \partial\Omega_{\text{Dirichlet}} \quad (4.4)$$

$$\langle \vec{\sigma}^l \rangle \cdot \vec{n} = \vec{N} \text{ on } \partial\Omega_{\text{Neumann}} \quad (4.5)$$

$$\text{with } \partial\Omega_{\text{Dirichlet}} \cup \partial\Omega_{\text{Neumann}} = \partial\Omega \quad (4.6)$$

We can comment on the strong form with the following recap points:

1. the liquid metal is Newtonian with a dynamic viscosity denoted  $\mu^l$
2. the metal is incompressible, therefore the liquid and solid densities are constant and equal (hence  $\rho_0^l$  in the inertial term) and the mass balance reduces to  $\nabla \cdot \langle \vec{v}^l \rangle = 0$
3. the Boussinesq approximation is used to compute the thermosolutal buoyancy force in the melt via the term  $g^l \langle \rho \rangle^l \vec{g} = g^l \langle \rho \rangle^l (T, \langle w_i \rangle^l) \vec{g}$ , where  $\langle \rho \rangle^l (T, \langle w_i \rangle^l)$  can be either tabulated as a function of temperature and liquid composition for each solute  $i$ , or directly approximated by:

$$\langle \rho \rangle^l = \rho_0^l \left( 1 - \beta_T (T - T_0) - \sum_{i=1}^{\text{nb species}} \beta_{w_i^l} (\langle w_i \rangle^l - \langle w_i \rangle_0^l) \right) \quad (4.7)$$

where  $\beta_T$  and  $\beta_{w_i^l}$  are respectively the thermal and solutal expansion coefficients, while  $T_0$  and  $\langle w_i \rangle_0^l$  represent a reference temperature and a reference liquid composition for each chemical species, respectively.

The weak form treated by the VMS solver derives from the strong form by multiplying

by test functions for velocity and pressure belonging to these functional spaces:

$$\begin{aligned} v &= \left\{ \vec{u}, \quad \vec{u} \in (\mathcal{H}^1(\Omega))^d \mid \vec{u} = \vec{v}_0 \text{ on } \partial\Omega \right\} \\ v^0 &= \left\{ \vec{u}, \quad \vec{u} \in (\mathcal{H}^1(\Omega))^d \mid \vec{u} = \vec{0} \text{ on } \partial\Omega \right\} \\ \varrho &= \{q, \quad q \in L^2(\Omega)\} \end{aligned}$$

where  $d$  stands for the space dimension. Then, based on these definitions, we write the advective upwinding stabilised test function for the velocity,  $\vec{U}$ :

$$\vec{U} = \vec{u} + \tau_{\text{SUPG}} \bar{\nabla} \vec{u} \cdot \left\langle \vec{v}^l \right\rangle_{\Omega_E} \quad (4.8)$$

$\tau_{\text{SUPG}}$  is an elemental stabilising parameter for advection-dominated terms and  $\left\langle \vec{v}^l \right\rangle_{\Omega_E}$  is the superficial velocity in the element  $\Omega_E$ , calculated by regular P1 interpolation:

$$\left\langle \vec{v}^l \right\rangle_{\Omega_E} = \frac{\sum_{i=1}^D \left\langle \vec{v}^l \right\rangle_i}{D} \quad (4.9)$$

Moreover, we need the following operators in order to simplify the notation of element-based variational integrals:

$$[a, b] = \int_{\Omega_E} ab \, d\Omega \quad (4.10)$$

$$[c, d]^* = \int_{\partial\Omega_E} cd \, d\Gamma \quad (4.11)$$

## Chapter 4. Macrosegregation with liquid metal motion

---

Finally, the SUPG-PSPG-LSIC stabilised weak formulation writes:

$$\left\{ \begin{array}{l} \forall \vec{u} \in v^0 \\ \left[ \left( \frac{\rho_0^l}{g^l} \frac{\partial \langle \vec{v}^l \rangle}{\partial t} \right), \vec{U} \right] + \left[ \left( \frac{\rho_0^l}{g^{l2}} (\bar{\nabla} \langle \vec{v}^l \rangle) \langle \vec{v}^l \rangle \right), \vec{U} \right] + \left[ \left( \frac{2\mu^l}{g^l} \right), \bar{\bar{\varepsilon}}(\langle \vec{v}^l \rangle) : \bar{\bar{\varepsilon}}(\vec{U}) \right] \\ + \left[ (\mu^l \mathbb{K}^{-1} \langle \vec{v}^l \rangle), \vec{U} \right] - \left[ (\langle \rho \rangle^l \vec{g}), \vec{U} \right] - [p, \nabla \cdot \vec{U}] - \left[ \frac{\vec{N}}{g^l}, \vec{U} \right]^* \\ + [\tau_{\text{LSIC}}, (\rho_0^l \nabla \cdot \langle \vec{v}^l \rangle \nabla \cdot \vec{u})] = 0 \\ \\ \forall q \in \varrho \\ \left[ \nabla \cdot \langle \vec{v}^l \rangle, q \right] + \left[ \tau_{\text{PSPG}} \frac{\vec{\nabla} q}{\rho_0^l}, \left( \frac{\rho_0^l}{g^l} \frac{\partial \langle \vec{v}^l \rangle}{\partial t} + \frac{\rho_0^l}{g^{l2}} (\bar{\nabla} \langle \vec{v}^l \rangle) \langle \vec{v}^l \rangle + \mu^l \mathbb{K}^{-1} \langle \vec{v}^l \rangle - \langle \rho \rangle^l \vec{g} \right) \right] = 0 \end{array} \right. \quad (4.12)$$

Replacing eq. (4.8) in eq. (4.12), we get the final weak form:

$$\left\{ \begin{array}{l} \forall \vec{u} \in v^0 \\ \left[ \left( \frac{\rho_0^l}{g^l} \frac{\partial \langle \vec{v}^l \rangle}{\partial t} \right), \vec{u} \right] + \left[ \left( \frac{\rho_0^l}{g^{l2}} (\bar{\nabla} \langle \vec{v}^l \rangle) \langle \vec{v}^l \rangle \right), \vec{u} \right] + \left[ \left( \frac{2\mu^l}{g^l} \right), \bar{\bar{\varepsilon}}(\langle \vec{v}^l \rangle) : \bar{\bar{\varepsilon}}(\vec{u}) \right] \\ + \left[ (\mu^l \mathbb{K}^{-1} \langle \vec{v}^l \rangle), \vec{u} \right] - \left[ (\langle \rho \rangle^l \vec{g}), \vec{u} \right] - [p, \nabla \cdot \vec{u}] - \left[ \frac{\vec{N}}{g^l}, \vec{u} \right]^* \\ + \left[ \tau_{\text{SUPG}} \bar{\bar{\nabla}} \vec{u} \cdot \langle \vec{v}^l \rangle_{\Omega_E}, \left( \frac{\rho_0^l}{g^l} \frac{\partial \langle \vec{v}^l \rangle}{\partial t} + \frac{\rho_0^l}{g^{l2}} (\bar{\nabla} \langle \vec{v}^l \rangle) \langle \vec{v}^l \rangle + \mu^l \mathbb{K}^{-1} \langle \vec{v}^l \rangle + \vec{\nabla} p^l - \langle \rho \rangle^l \vec{g} \right) \right] \\ + [\tau_{\text{LSIC}}, (\rho_0^l \nabla \cdot \langle \vec{v}^l \rangle \nabla \cdot \vec{u})] = 0 \\ \\ \forall q \in \varrho \\ \left[ \nabla \cdot \langle \vec{v}^l \rangle, q \right] + \left[ \tau_{\text{PSPG}} \frac{\vec{\nabla} q}{\rho_0^l}, \left( \frac{\rho_0^l}{g^l} \frac{\partial \langle \vec{v}^l \rangle}{\partial t} + \frac{\rho_0^l}{g^{l2}} (\bar{\nabla} \langle \vec{v}^l \rangle) \langle \vec{v}^l \rangle + \mu^l \mathbb{K}^{-1} \langle \vec{v}^l \rangle + \vec{\nabla} p^l - \langle \rho \rangle^l \vec{g} \right) \right] = 0 \end{array} \right. \quad (4.13)$$

### 4.3.2 Stabilisation parameters

Several expressions for  $\tau_{\text{SUPG}}$  were derived by Tezduyar et al. [1992] and Tezduyar and Osawa [2000], from which we retain the following:

$$\tau_{\text{SUPG}} = \left( \frac{1}{\tau_{\text{advec}}^2} + \frac{1}{\tau_{\text{diff}}^2} + \frac{1}{\tau_{\text{trans}}^2} \right)^{-1/2} \quad (4.14)$$

where we use three parameters  $\tau_{\text{advec}}$ ,  $\tau_{\text{diff}}$  and  $\tau_{\text{trans}}$  having time as unit ( $s$ ) that stabilise respectively advection-dominated, diffusion-dominated and transient-dominated regimes, given by:

$$\tau_{\text{advec}} = \frac{h_{\text{stream}}}{2\|\langle \vec{v}^l \rangle_{\Omega_E}\|} \quad (4.15)$$

$$\tau_{\text{diff}} = \frac{h_{\text{stream}}^2}{4\nu^l} \quad (4.16)$$

$$\tau_{\text{trans}} = \frac{\Delta t}{2} \quad (4.17)$$

where  $h_{\text{stream}} = 2\|\langle \vec{v}^l \rangle_{\Omega_E}\| \left( \langle \vec{v}^l \rangle_{\Omega_E} \cdot \vec{\nabla} \mathcal{P} \right)$  is the element length in the stream direction, computed using the local superficial velocity and the interpolation functions  $\mathcal{P}_j$  relative to each local node  $j$ ,  $\nu^l$  is the liquid's kinematic viscosity ( $\text{m}^2 \text{s}^{-1}$ ) and  $\Delta t$  is the time step. The transient term stabilisation was initially derived for Navier-Stokes equations without Darcy term. As the latter has a significant role in the weak form eq. (4.13), it needs to be stabilised. The current thesis is based on several past projects that either considered eq. (4.17) like Liu [2005] or modified it like Gouttebroze [2005] and Rivaux [2011] to take account the Darcy term, giving the term:

$$\tau_{\text{trans-darcy}} = \frac{\Delta t}{2 \left( 1 + \Delta t \frac{\mu^l}{\rho_0^l \mathbb{K}} \right)} \quad (4.18)$$

In the literature, no substantial references were found to backup the formulation of eq. (4.18), it will be used in the current work though. It is worth mentioning that Zabaras and Samanta [2004] has invoked the necessity to stabilise Darcy terms in a generalised Navier-Stokes/Darcy P1/P1 formulation, and introduced what they call Darcy-Stabilising/Petrov-Galerkin (DSPG), using local non-dimensional numbers of Darcy ( $Da$ ) and Prandtl ( $Pr$ ) numbers expressing respectively the ratio of local permeability to a characteristic length  $L$  and the ratio of momentum diffusivity,  $\nu^l$ , to heat

## Chapter 4. Macrosegregation with liquid metal motion

---

diffusivity in the liquid,  $\alpha^l$ :

$$\tau_{\text{darcy}} = \frac{Da}{Pr} \left( \frac{g^l}{1 - g^l} \right)^2 = \frac{\alpha^l \mathbb{K}}{\nu^l L^2} \left( \frac{g^l}{1 - g^l} \right)^2 \quad (4.19)$$

Last, the definitions of the remaining stabilisation parameters are given as follows:

$$\tau_{\text{PSPG}} = \tau_{\text{SUPG}} = \left( \left( \frac{2 \|\langle \vec{v}^l \rangle_{\Omega_E} \|}{h_{\text{stream}}} \right)^2 + \left( \frac{4 \nu^l}{h_{\text{stream}}^2} \right)^2 + \left( \frac{2 \left( 1 + \Delta t \frac{\mu^l}{\rho_0^l \mathbb{K}} \right)}{\Delta t} \right)^2 \right) \quad (4.20)$$

$$\tau_{\text{LSIC}} = \frac{h_{\text{stream}}}{2} \|\langle \vec{v}^l \rangle_{\Omega_E} \| Z(Re_{\Omega_E}) \quad (4.21)$$

with  $Z(Re_{\Omega_E})$  being a local Reynolds-dependant function that evaluates to:

$$Z(Re_{\Omega_E}) = \begin{cases} Re_{\Omega_E}/3 & \text{if } Re_{\Omega_E} \leq 3 \\ 1 & \text{if } Re_{\Omega_E} > 3 \end{cases} \quad (4.22)$$

and

$$Re_{\Omega_E} = \frac{\|\langle \vec{v}^l \rangle_{\Omega_E} \| h_{\text{stream}}}{2 \nu^l} \quad (4.23)$$

### 4.3.3 Implementation

The final matrix definition of the weak form of eq. (4.3) is given by:

$$\begin{pmatrix} A_{vv} & A_{vp} \\ A_{pv} & A_{pp} \end{pmatrix} \begin{pmatrix} \langle \vec{v}^l \rangle \\ p^l \end{pmatrix} = \begin{pmatrix} B_v \\ B_p \end{pmatrix} \quad (4.24)$$

### CFL condition

### Integration order

Using P1 linear elements implies a P2 integration ? what are the advantages (time) and limitations ?

## 4.4 Application to multicomponent alloys

### 4.4.1 *Tsolver* validation with fluid flow

To validate the *Tsolver* with fluid flow, we consider the following set of equations already defined in the flowchart of [section 2.1.1](#). Moreover, an assumption of a static and non deformable solid phase is made. Consequently, the mechanical model is reduced to the conservation of momentum in the liquid phase.

The *Tsolver*'s ability to be coupled with various physical phenomena like macrosegregation and fluid flow in porous medium is validated using an experimental solidification benchmark. The validation case consists of a 10 cm width  $\times$  6 cm height  $\times$  1 cm thick crucible containing a Sn-3 wt.% Pb melt. The alloy is cooled down from its two narrowest vertical sides using heat exchangers (LHE: left heat exchanger, RHE: right heat exchanger). The experiment, inspired by [Hebditch and Hunt \[1974\]](#) similar set up, has been revisited by [Hachani et al. \[2012\]](#) who performed the solidification with better controlled conditions and using an increased number of samples for composition analysis. Recently, a successful attempt to simulate the experiment was carried out by [Carozzani et al. \[2013\]](#) relying on an enthalpy resolution. All details regarding geometry, finite element discretization, material properties and boundary conditions can be found in the latter reference.

For this computation, solidification paths, phase compositions and phase enthalpies were determined by a thermodynamic module dedicated to equilibrium calculations for binary alloys. The 3D simulation results in [fig. 4.2](#) show a satisfactory agreement with the experimental temperature measurements recorded at mid-heights of the cavity and uniformly distributed along its width.

Furthermore, simulation results with the *Tsolver* and the *Hsolver* previously obtained by [Carozzani et al. \[2013\]](#) were found to be almost superimposed. This is confirmed by a comparison made between both solvers, as shows [fig. 4.3](#), where the average composition, liquid fraction and temperature fields are extracted from a cut plane halfway through the ingot. On the same figure, if we compare the composition, we notice that the solidified part on the RHE side has basically the same segregation pattern, while the convected liquid has a slightly different solute distribution. As for the extent of the mushy zone, we observe that liquid fraction contours are very close, indicating that temperature distributions and interdendritic segregation are also close between both solvers predictions.

Regarding the computation, the *Tsolver* resolution proves to be faster than the *Hsolver* used by [Carozzani et al. \[2013\]](#): a process time of 7000s required a computation time of 90 hours 13 minutes compared to 114 hours 21 minutes spent by the enthalpy

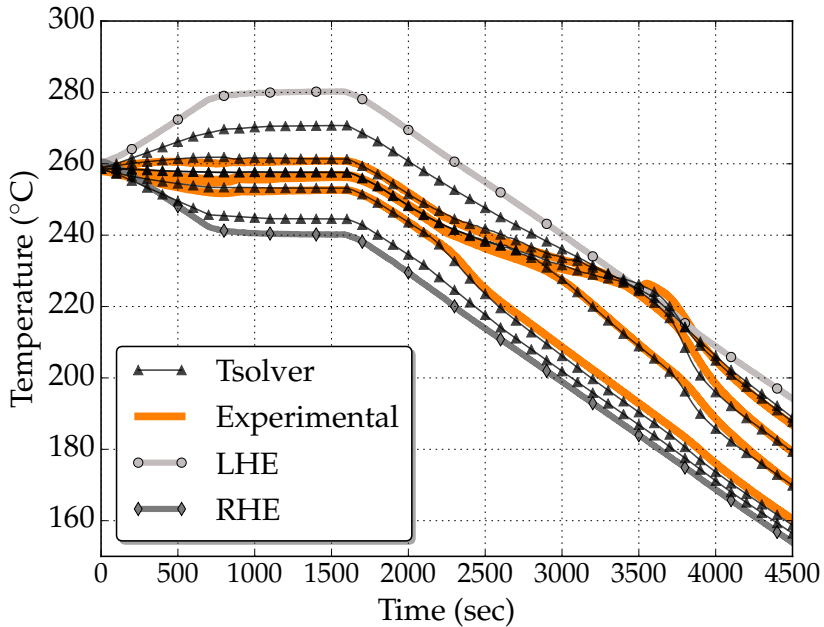


**Fig. 4.2** – Results of the 3D FE convection-diffusion simulation, overlapping with the experimental cooling curves. The left (LHE) and right (RHE) heat exchangers impose the boundary temperature in the experiment.

resolution with 32 cores on the same cluster. The gain factor is about 20%.

In the previous chapter, we have considered a static melt upon solidification of multi-component alloy. The artificial consideration of a still flow is dropped in this chapter, hence taking into account macrosegregation caused by fluid motion, using realistic values of the expansion coefficients given in [table 3.3](#). In the real conditions, the melt is in constant motion and knowing that the carbon and chromium solutes have lightening effects on the liquid at nominal composition, the density inversion resulting from the composition gradient in the interdendritic liquid, may cause flow instability (segregation plumes) at the solidification front. While the selected alloy is a steel, this application is also representative of directional cooling in a single crystal casting, e.g. for nickel-base superalloys [[Beckermann et al. 2000](#)]. Solidification of this class of alloys is carefully controlled so as to prevent any freckle-type defect to exist in the as-cast state. In this section, we consider the same simulation parameters defined in [table 3.3](#) as well the geometry and thermal boundary conditions previously defined in [fig. 3.6](#). Moreover, we solve the liquid momentum conservation equation, with non-slip boundary conditions on all external sides of the cylinder.

#### 4.4. Application to multicomponent alloys

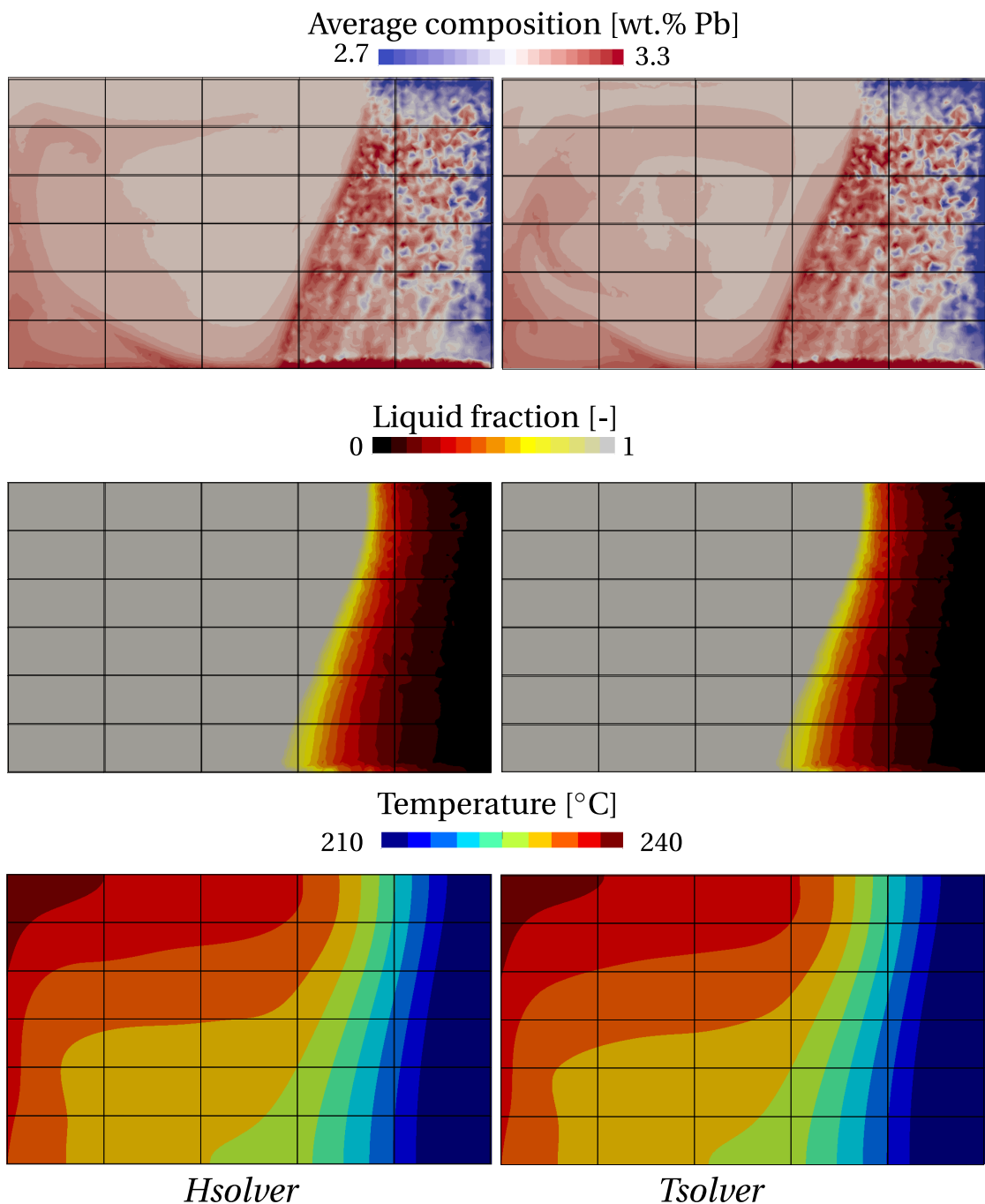


**Fig. 4.3 – Comparison of 3D simulation results: average composition, liquid fraction and temperature at  $t=3000$  s for *Tsolver* and *Hsolver*.**

### 4.4.2 Results

Solidification starts at 407 s when the cylinder's bottom base temperature reaches the liquidus temperature of the alloy. In fact, the solidification onset is the same as in the pure diffusion case in [fig. 3.9](#), since the average composition remains unchanged for an entirely liquid domain (assuming an initially infinite solute mixing in the melt).

As shown in [fig. 4.4](#) at 600 s, the first solid phase to form remains ferrite. We can also see solute-rich channels forming in the mushy zone and solute plumes rising in the melt above the mushy zone due to a subsequent upward flow. It is actually caused by the thermosolutal buoyancy force created by the carbon and chromium solutes. Such phenomenon could delay solidification inside liquid-rich channels and results in a freckling defect [Felicelli et al. 1991] on the surface of the cylinder as well as inside, as shown later in this section. As solidification proceeds, the liquid becomes more enriched with solute and the peritectic reaction forming the austenite phase is reached. However, for very large enriched melt, it can also be observed that primary solidification proceeds with the austenite phase rather than the ferrite phase. The carbide phase can also form with the austenite phase at some locations. These observations correspond to a simulation time of 2000 s in [fig. 4.4](#).

Solidification ends at around 2475 s, the last liquid solidifying at the cylinder's top surface, where the average composition reaches a maximum of Fe-2.151 wt.% C-30.633 wt.% Cr, i.e. a relative positive macrosegregation,  $(\langle w_i \rangle - \langle w_i \rangle_0) / \langle w_i \rangle_0$ , of 7.5% for carbon and 2.1% for chromium. The fact that the maximum average composition is observed at the top, is verified in [fig. 4.5a](#) which shows the composition map in a 2D vertical slice through the longitudinal axis of the cylinder. We can also see it in [fig. 4.5b](#) where the relative composition profile are plotted at the end of the cooling process along the longitudinal cylinder axis Z-Z' and along the axis of the segregated channel, F-F'. The negative segregation up to 1 cm from the chill corresponds to the solute depletion caused by the first solid formation. The subsequent solidification enriches further the liquid; hence the solid composition also increases.

The composition evolution trend for both solutes is similar: an overall rise until positive segregation is achieved above 5 cm from the chill. The positive macrosegregation intensifies when the profile is chosen at the center of the segregated channel, negative segregation then becoming less pronounced.

#### 4.4. Application to multicomponent alloys

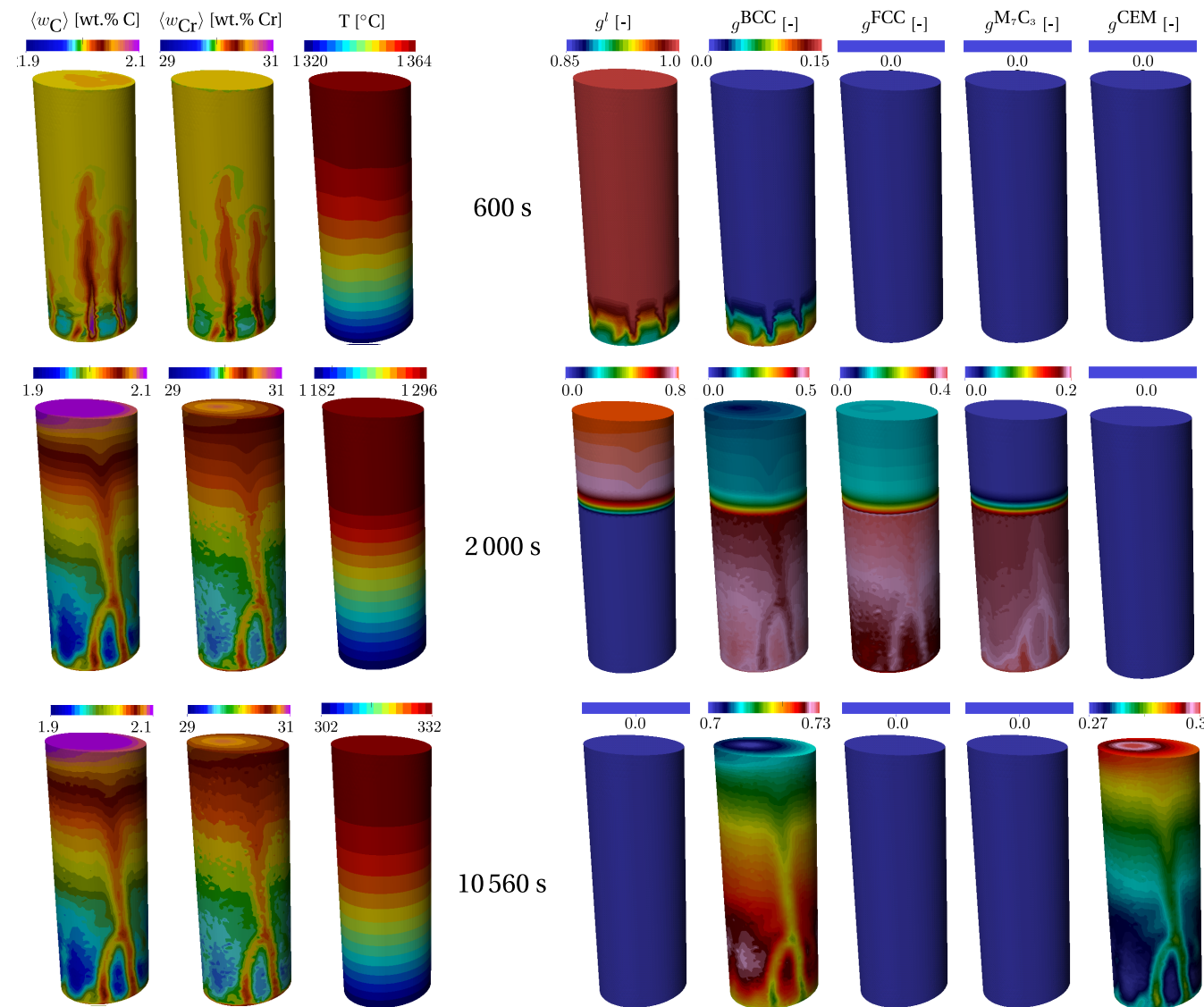


**Fig. 4.4 –** Upward solidification of a cylinder rod at 3 stages showing the metallurgical consequences of macrosegregation Fe-2 wt.% C-30 wt.% Cr. The left columns show the average composition and temperature distribution, while the right columns show the phase fractions.

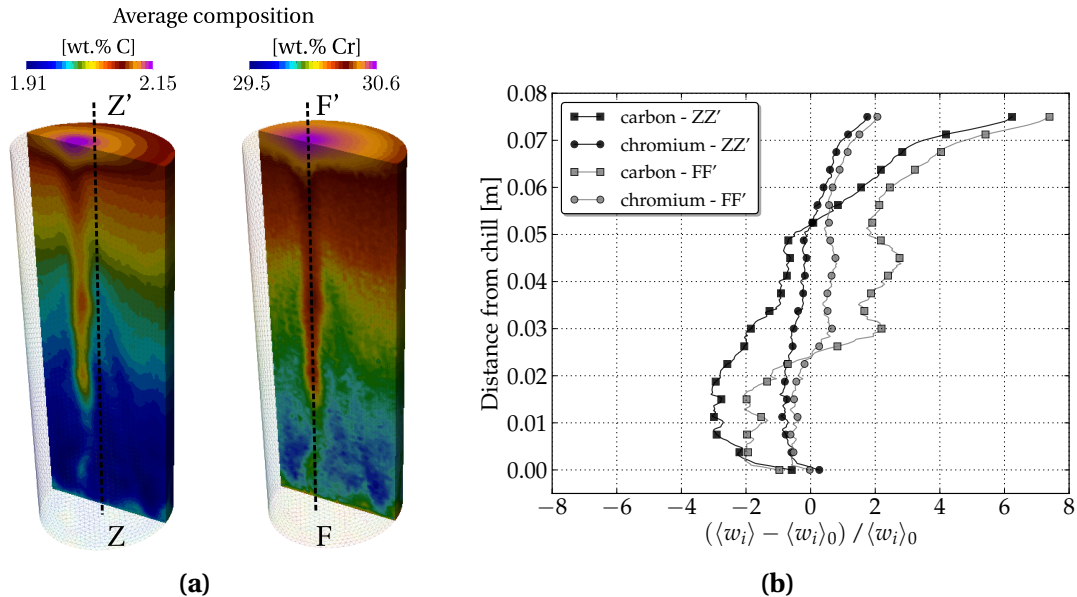


**Fig. 4.5** – (a) average composition map on a vertical section inside the sample, with (b) relative macrosegregation profiles on the vertical revolution axis.

Beyond 2475 seconds, no variations of the average composition maps are observed since solute diffusion in the solid phases is neglected. Nonetheless, as temperature decreases, solid-state transformations are still possible as for the case with no macrosegregation. The formation of a cementite phase begins at the cylinder base at 8843 s with a temperature of 496.9 °C. At about 9293 s, the isotherm 488.5 °C reaches the top surface. This temperature value is the local cementite solvus temperature. The difference in the solvus temperature between the bottom and top surfaces is due macrosegregation. Macrosegregation also explains the variation in the cementite content. The solid state transformation ends shortly before 10 500 s. The influence of the solidification process is clear on the final macrosegregation pattern, hence the final phase distribution. This is better illustrated by drawing the time evolution of phase fractions at the center of the bottom and top surfaces of the cylinder in fig. 4.6. With no macrosegregation, in fig. 4.6a, the final distribution of the phases is the same at time 12 000 s, while with macrosegregation, in fig. 4.6b, variations of the cementite and ferrite are revealed. The segregated channels inside the cylinder and on the boundary, are often termed *freckles* when they consist of visible equiaxed grains [Copley et al. 1970]. This defect is marked by a noticeable gradient of composition and phase fractions, possibly changing the mechanical properties in the channels, hence the overall mechanical behaviour of the alloy. The coupling of the Tsolver with thermodynamic tabulations is thus demonstrated. It shows the ability to predict complex solidification paths, even if only at equilibrium. As for the computation time, the Tsolver resolution performed

better: 500 seconds of solidification required 6 hours 14 minutes compared to 8 hours 6 minutes spent by the enthalpy resolution with 12 cores on the same machine. The gain factor is about 22%.

## 4.5 Macroscopic prediction of channel segregates

### 4.5.1 Introduction

We have seen in the previous multicomponent solidification test case, a formation of segregated channels in the cylinder. This defect manifests itself as a composition inhomogeneity that is highly non-isotropic. A typical description of its morphology would consider a channel with a diameter proportional to few primary dendrite arm spacing and a length that could vary from millimeters to centimeters. These “worm”-like shapes could form during directional solidification of cast parts designed for engine applications, particularly in Nickel-base superalloys [Giamei and Kear 1970; Becker-mann et al. 2000; Genereux and Borg 2000; Schneider et al. 1997]. In the latter situation, the channels are filled with a chain of small equiaxed crystals, thus referring to the term “freckle”. In large steel ingots, these channel defects are also related to A- and V-segregates [Pickering 2013].

Considering a binary alloy with a partition coefficient less than unity and having a negative liquidus slope, freckles may form by the following mechanisms: i) solute partitioning occurs at the scale of dendrite arms and solute is rejected in the melt, ii) local composition gradients are intensified resulting in an increase of the solutal buoyancy force in the mushy zone, iii) solute-rich pools are formed, causing segregation chimneys and convective plumes in the melt, iv) which lead to partial remelting and transport of dendrites, continuous solute feeding and locally delayed solidification, and finally v) accumulation of fragments and/or equiaxed crystals in the chimneys before the end of solidification.

Because it is of prime importance to control the occurrence of channel segregation, several attempts have been made from the late 1960's [Flemings and Nereo 1967; Flemings et al. 1968; Flemings and Nereo 1968] to the early 2000's [Ramirez and Becker-mann 2003] to understand it and characterise it by deriving freckling criteria. These studies are summarized in [Auburtin 1998]. One of the reasons for only considering freckling criteria is that direct realistic simulations of the formation of freckles in a casting geometry are still difficult. Indeed, experimental observations show that it requires a satisfying description of the microstructure together with the 3D convective flow controlled by the cooling conditions of the complete cast part [Shevchenko

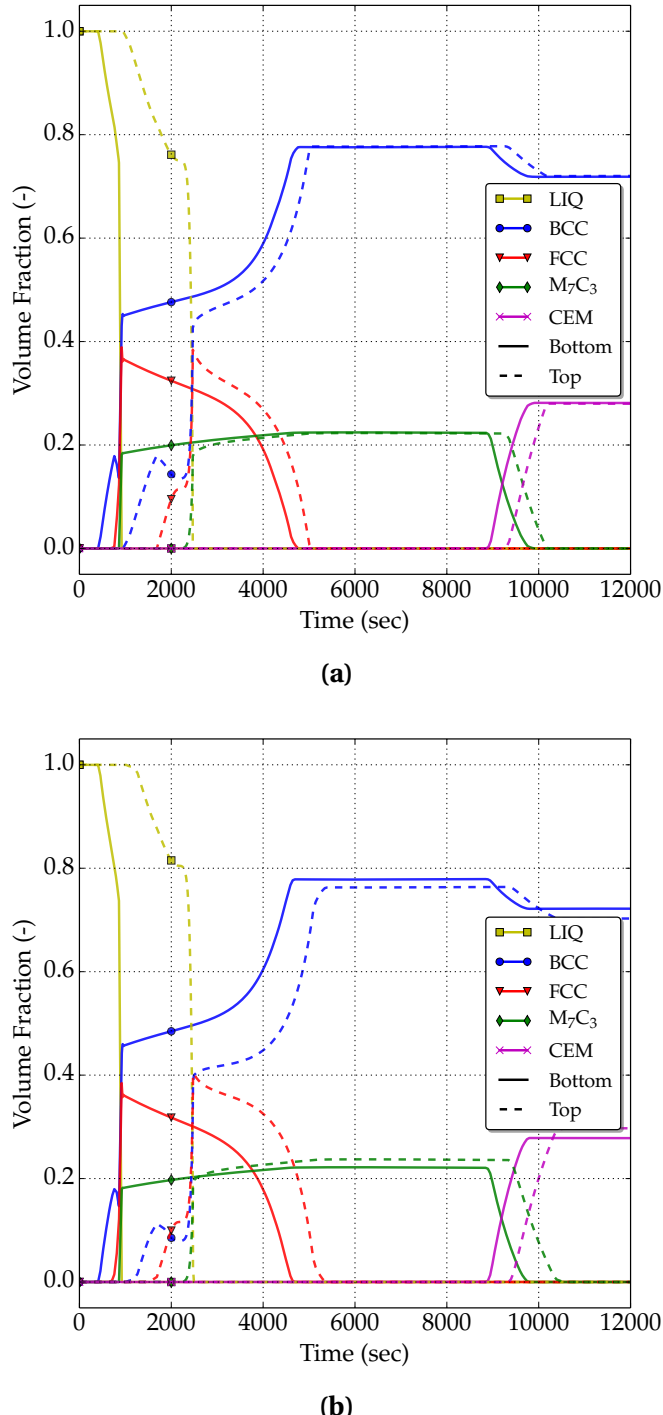


**Fig. 4.6** – History of phase fraction (a) without macrosegregation and (b) with macrosegregation at the center of the (plain) bottom and (dashed) top surfaces of the cylinder surfaces, extracted from simulations displayed in (a) [fig. 3.9](#) and (b) [fig. 4.4](#).

et al. 2013]. Such information is not accessible yet. Only simulations in representative simple cuboid or cylindrical domains are usually achieved [Felicelli et al. 1991; Felicelli et al. 1998; Kohler 2008; Guo and Beckermann 2003], except when considering small volume casting [Desbiolles et al. 2003]. They are usually limited to unstable thermosolutal convection without or with little regard to the microstructural features. Considering the spatial resolution of the defect, being for example of the order of the primary dendrite arm spacing, a fluid flow computation in the 3D casting part is also very demanding and not common in the literature. Among other criteria, the dimensionless Rayleigh number has been identified as a good indicator for the occurrence of segregation channels or a subsequent freckle defect. The dependence of freckling tendency on the Rayleigh number has been studied numerically and compared to experimental observations, as done by [Ramirez and Beckermann 2003].

### 4.5.2 Experimental work

An interesting experimental work on directional solidification of In-75 wt.% Ga featuring in-situ X-ray monitoring has been recently carried out by Shevchenko et al. [2013]. The comparison with numerical modelling is paramount for two main reasons: firstly, the in-situ technique allows to follow solidification in real-time and offers visual description of the system behaviour: grain morphology, composition evolution, effect on fluid flow in the mushy zone and chimney initiation, as well as other modelling input data such as dendritic and eutectic nucleation undercooling; secondly, an indium-gallium system is more representative of metallic alloy solidification than the widely used organic systems, e.g. the succinonitrile-acetone mixture that exhibits alloy-like dendritic formation in its growth stage. Further information with respect to the experimental hardware, procedure and data analysis can be found in [Boden et al. 2008; Shevchenko et al. 2013].

### 4.5.3 Macroscopic scale simulations

#### Configuration

The focus of this section is on qualitative comparison between numerical simulation and the previously mentioned experiment. The experimental cell geometry shown in fig. 1.7c is hexagonal. With adiabatic lateral sides, it results in a bending of the isotherm surfaces as shown in the experiment. The metallic cooling plates shown in fig. 4.7a partly compensate for this effect. However, a residual horizontal component of the temperature gradient remains. To qualitatively replicate this effect while simplifying the cell geometry, a 22 mm × 22 mm × 1 mm cuboid cell is considered with

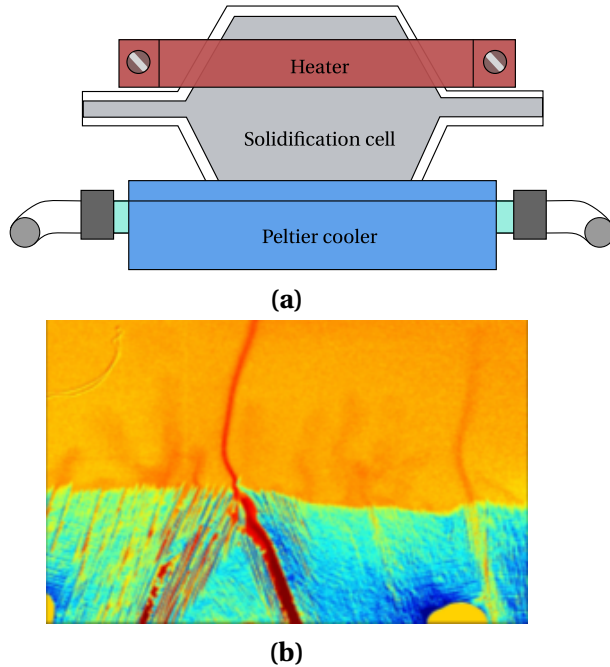


**Fig. 4.7** – Illustration of the benchmark experiments for in-situ observation of segregated channels formation using X-Ray radiography with (a) a schematic of the cell and (b) a typical image of the microstructure formed during directional solidification of an In-75 wt.% Ga alloy. Reproduced from [Shevchenko et al. 2013].

small cooling fluxes on its lateral vertical side surfaces computed using a constant heat transfer coefficient,  $h_{ext}$ , and a constant environment temperature,  $T_{ext}$ . Temperatures at the bottom and top surfaces, respectively  $T_{Top}$  and  $T_{Bottom}$ , are imposed in a way to maintain a constant vertical gradient,  $G$ , thus linearly decreasing over time with the same cooling rate  $R$ . Both square faces of the geometry, having an area of  $22\text{ mm} \times 22\text{ mm}$ , are adiabatic. In spite of taking cell dimensions similar to benchmark experiments presented above, the cell thickness is increased from  $150\text{ }\mu\text{m}$  to  $1\text{ mm}$ . This facilitates the computation and will later be subject to discussion.

**Table 4.1** – Summary of the simulations and the corresponding parameters for the FE cases, where a purely macroscopic model is used. Parameters are varied from (G1) low to (G2) high gradient and (L0) no, to (L1) low lateral cooling.

Case	Vertical gradient $G$ [ $\text{K mm}^{-1}$ ]	Cooling rate $R$ [ $\text{K s}^{-1}$ ]	Lateral cooling $L$ ( $h_{ext}, T_{ext}$ ) [ $\text{W m}^{-2} \text{K}^{-1}, ^\circ\text{C}$ ]	Initial temperature ( $T_{top}, T_{bottom}$ ) [ $^\circ\text{C}$ ]
FE-G1R1L0	G1:0.2	R1:-0.01	L0:(0,0)	(29.75, 25.25)
FE-G1R1L1	G1:0.2	R1:-0.01	L1:(20,0)	(29.75, 25.25)
FE-G2R1L1	G2:1.5	R1:-0.01	L1:(20,0)	(58.25, 25.25)

Materials properties are provided in [table 4.2](#) while initial and boundary conditions

are given in [table 4.1](#). A series of computations is performed to understand the influence of process parameters on the final macrosegregation pattern. In directional growth, the main parameters are the vertical temperature gradient,  $G$ , and the cooling rate,  $R$ , since they control the isotherms speed. However, the effect of a higher lateral cooling is also considered below by increasing the heat transfer coefficient,  $h_{\text{ext}}$ . Finally, the grain structure is another crucial parameter that drastically changes the analysis inasmuch as growth undercooling is fundamental to determine the onset of solidification. The computation cases used in this study are presented in [table 4.1](#). The label of each case allows direct access to the simulation parameters as explained in the caption. Values for these parameters are inspired from the above experiments ([section 4.5.2](#)). Initial conditions consider a quiescent liquid at uniform composition given by the nominal alloy composition  $\langle w_0 \rangle$ . The temperature field is also initially uniform at a temperature averaged between the top and bottom initial values provided in [table 4.1](#). It has been checked that a uniform temperature gradient is swiftly reached, and that the unsteady regime to settle a vertical temperature gradient does not affect the phenomena studied. For simulations with grain structures, boundary conditions for nucleation at the bottom horizontal  $22 \text{ mm} \times 1 \text{ mm}$  surface are kept constant as given in [table 4.1](#).

The macroscale approach employs the finite element method to compute the temperature and composition fields at FE nodes. The liquid fraction is then determined directly from the former fields, assuming a linear phase diagram, i.e. linear liquidus with full thermodynamic equilibrium between phases or lever rule approximation. This linear approximation is made available by the dotted line provided in [fig. 4.8](#). Note that this line defines a phase diagram that seems very different from the correct one. However, this linear fit is only used in a composition region located around the nominal composition of the alloy. It is also worth noticing that the eutectic microstructure is expected to appear at  $15.3^\circ\text{C}$ . However, experimental observations revealed that large eutectic nucleation undercooling was reached, so the eutectic solidification was not reported in the experiments studied by [Shevchenko et al. \[2013\]](#). Consequently, the solidification path is computed without accounting for the eutectic microstructure in the present simulations, thus extending the liquidus and solidus lines below the eutectic temperature as sketched with the linear approximations in [fig. 4.8](#).

## Results

The first case labeled FE-G1R1L0 is a reference case that features a low gradient (G1), low cooling rate (R1), and without any lateral cooling (L0), ensuring that isotherms

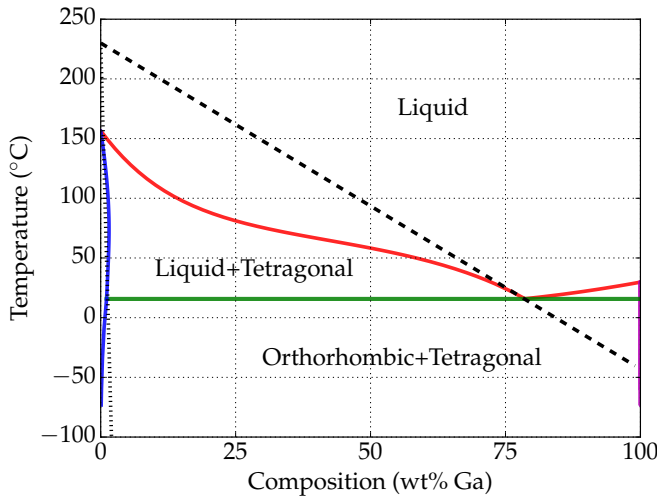
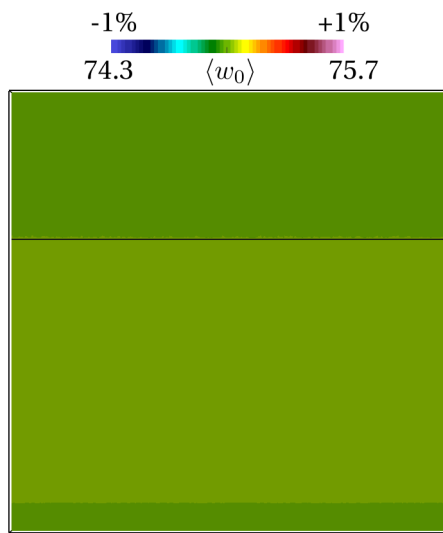


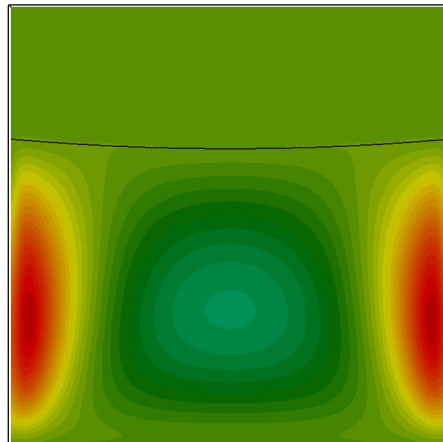
**Fig. 4.8** – Binary phase diagram of the In-Ga system [Andersson et al. 2002; TCBIN 2006] and its approximation for solidification studies with an In-75 wt.% Ga alloy. The dashed and dotted lines are linear liquidus and solidus approximations near the nominal composition.

retain a planar shape. These simulation parameters defined in [table 4.2](#), result in a negligible fluid flow reaching a maximum velocity of  $4 \times 10^{-8} \text{ mm s}^{-1}$  in the bulk. Accordingly, the solidification front remains stable and follows the planar isotherms; no chimneys are observed. The average composition field is thus only little modified in the mushy zone as shown in [fig. 4.9](#) (mind the values of the scale limits). It is concluded that velocity in the bulk is not high enough to initiate instabilities. In the next case, FE-G1R1L1, a cooling flux with a constant and very low value of the heat transfer coefficient is imposed on both vertical lateral surfaces to initiate a downward fluid flow by thermal buoyancy. Once solidification starts, solute-rich regions start to appear on the sides of the domain. Despite the visible concentration difference between these lateral regions and the central mush seen in [fig. 4.9](#), their diffuse and uniform aspect indicates no resemblance to segregated channels. We keep the same configuration but increase the vertical gradient from  $0.2 \text{ K mm}^{-1}$  (G1) to  $1.5 \text{ K mm}^{-1}$  (G2) in the case FE-G2R1L1. The isotherms become closer to each other hence reducing the depth of the mushy zone for the same time increment compared to the preceding case. The rejected gallium solute locally accumulates at several different positions in the mushy zone, stemming from the base of the cell, with a maximum of 0.7 wt.%Ga above nominal composition. This is the consequence of segregation of gallium rich liquid being lighter than the above liquid bulk and creating an upward buoyancy force. The positive segregation and subsequent Ga-rich chimneys then rise up with an upward velocity component slightly greater than  $1 \text{ mm s}^{-1}$ . [Figure 4.10](#) gives a series of snapshots for case FE-G2R1L1 at three different times. Among the two clear distinct

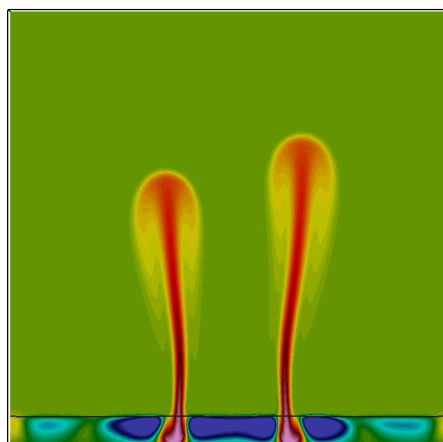
#### 4.5. Macroscopic prediction of channel segregates



(a) FE-G1R1L0



(b) FE-G1R1L1



(c) FE-G2R1L1

**Fig. 4.9** – Average Ga composition field at 250 s for the 3 FE cases showing the influence of process parameters on the freckling tendency. The black line represents the liquidus isotherm given in [table 4.2](#).

## Chapter 4. Macrosegregation with liquid metal motion

---

**Table 4.2** – Material parameters for In-75 wt.% Ga and numerical parameters.

Parameter	Symbol	Value	Unit
Nominal composition	$\langle w_0 \rangle$	75	wt.%
Liquidus temperature	$T_l$	25.25	°C
Segregation coefficient	$k$	0.0165	wt.% wt.% <sup>-1</sup>
Liquidus slope	$m_l$	-2.73	K wt.% <sup>-1</sup>
Gibbs-Thomson coefficient	$\Gamma_{GT}$	$2 \times 10^{-7}$	K m <sup>-1</sup>
Heat capacity (liquid and solid)	$C_p$	380.74	J kg <sup>-1</sup> K <sup>-1</sup>
Enthalpy of fusion	$L$	$8.02 \times 10^{-4}$	J kg <sup>-1</sup>
Diffusion coefficient of Ga in liquid In	$D^l$	$1.525 \times 10^{-9}$	m <sup>2</sup> s <sup>-1</sup>
Dynamic viscosity	$\mu^l$	$2 \times 10^{-3}$	Pa s
Thermal expansion coefficient	$\beta_T$	$0.0978 \times 10^{-3}$	K <sup>-1</sup>
Solutal expansion coefficient	$\beta_{\langle w \rangle^l}$	$1.44 \times 10^{-3}$	wt.% <sup>-1</sup>
Thermal conductivity in the solid	$\langle \kappa \rangle^s$	40	W m <sup>-1</sup> K <sup>-1</sup>
Thermal conductivity in the liquid	$\langle \kappa \rangle^l$	28	W m <sup>-1</sup> K <sup>-1</sup>
Dendrite arm spacing	$\lambda$	$60 \times 10^{-6}$	m
Density	$\rho_0^l$	6725	kg m <sup>-3</sup>
Reference composition	$w_0^l$	75	wt.%
Reference temperature	$T_0$	25.25	°C
CA cell size		$30 \times 10^{-6}$	m
FE mesh size		$140 \times 10^{-6}$	m
Time step	$\Delta t$	0.1	s

plumes that are visible at 250 s in [fig. 4.9](#), only one has led to a channel formation, that remains in [fig. 4.10](#) at 500 s. In fact, an animation between 250 s and 500 s (not shown here) reveals that one plume vanishes, thus permitting the first one to further develop. A second freckle is also seen on the left hand side of the cell. These two freckles are stable for a long time since they remain at time 1000 s. However, the left side freckle develops further to become the main one at 1500 s, while the mid-width freckle decreases in intensity, changes orientation and subsequently disappears (not shown here). Thus, the birth and death of very few freckles is observed in this simulation, mainly due to solutal instability, as the temperature field shown in [fig. 4.10](#) clearly remains stable despite the low lateral heat flux. As shown in [fig. 4.9](#), instability is yet required to create these chemical plumes and channels. Here, it is created by a very small lateral heat flow but other sources of instability could be involved, as shown with the grain structure in the next section.

---

#### 4.5. Macroscopic prediction of channel segregates

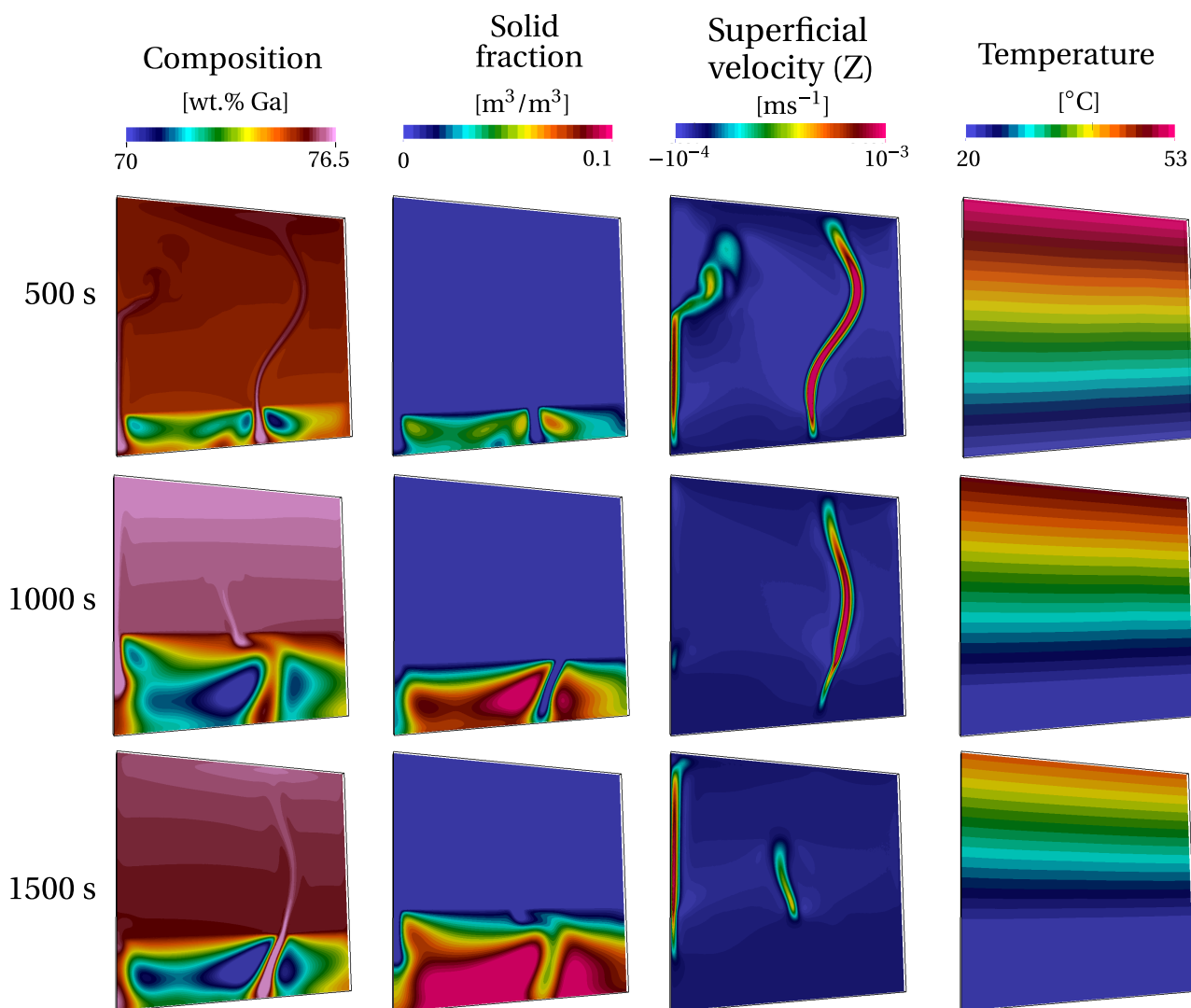


**Fig. 4.10** – Simulation results for case FE-G2R1L1 showing maps of the average composition in gallium, the solid fraction, the superficial velocity field (vertical component) and the temperature, on a cut plane at the center of the cell at 500 s, 1000 s and 1500 s.

### Discussion

In section 4.5.1, we have introduced some successful attempts of freckle predictions. The authors tackled the problem from an qualitative perspective. To our knowledge, the closest work to quantitative freckling analysis in solidification literature was done by Ramirez and Beckermann [2003]. They attempted to draw a correlation (freckling criterion) between the process parameters and the occurrence of freckles, without any size or shape constraints, i.e. any flow instability that may appear and form the smallest freckle is considered.

To accomplish this, they took a number of experiments done independently by Pollock and Murphy [1996] and Auburtin et al. [2000] where the casting parameters vary one at a time: casting speed ( $R$ ), thermal gradient ( $G$ ), angle ( $\theta$ ) with respect to vertical orientation and nominal composition ( $\langle w_0 \rangle$ ), giving a database for 6 different superalloys. The experimental results were compared to a modified Rayleigh number that accounts for the various parameters. It allowed them to define a threshold for freckle formation in Nickel-base superalloys, as well as Pb-Sn alloys.

Other contributions by Yuan and Lee [2012] (Pb-Sn alloy) and Karagadde et al. [2014] (In-Ga alloy) relied on a Cellular Automata Finite Difference (CAFD) model developed by Lee et al. [2002], which solves the dendrite tip growth kinetics at the solid-liquid interface together with macroscopic conservation equations. The authors compared the simulated formation of freckles with the results obtained by Shevchenko et al. [2013]. However, these simulations follow solidification in a small volume that contains a few dendrites with interdendritic liquid, therefore limited as far as to predict the liquid behaviour outside the mushy zone. On another hand, experimental observations reveal a great deal of information regarding solute redistribution, first in the chimneys that wash the dendrites in their way and then convective plumes that expel chemical species outside the mush, resulting in a global complex phenomenon.

In order to capture simultaneously the interaction between the mushy zone and the free liquid, we use the Cellular Automata Finite Element (CAFE) method to combine the macroscopic and mesoscopic length scales and predict more realistic channel segregation.

# 4.6 Meso-Macro prediction of channel segregates

## 4.6.1 Numerical method

### **Microscopic scale**

The CAFE model introduces a grid of regular and structured cubic cells, with a constant size in all space directions, referred to as the cellular automaton (CA) grid. It is different from the unstructured finite element mesh previously mentioned for the solution of the average conservation equations. A typical CA step dimension is smaller than the smallest FE mesh size. The CA grid serves to represent solidification phenomena including nucleation, growth and remelting of the envelope of the primary dendritic grains. Details about the CAFE model can be found in [Carozzani et al. 2012; Carozzani et al. 2013; Carozzani et al. 2014]. Cell information, such as the temperature, the average composition or the velocity of the liquid phase, is interpolated from the nodes of the FE mesh. State indices are also defined for each CA cell, providing the presence of liquid or solid phases.

### **Nucleation**

Initially, cells are in a fully liquid state. In the present situation, random nucleation sites are chosen based on a nucleation density,  $n_{\max}$  (expressed in surface density inverse m<sup>-2</sup>), at the bottom surface of the geometry in contact with the cooler. Nucleation occurs in a cell only if the latter contains a nucleation site, and when the local undercooling of the cell reaches the critical nucleation undercooling given as input by a Gaussian distribution of mean undercooling  $\Delta T_N$  with a standard deviation  $\Delta T_\sigma$ . The crystallographic orientation of each grain newly nucleated is also randomly chosen using values of the Euler angles to fully define the three rotations that transform the reference frame to the ⟨100⟩ directions that define the main growth axes of the dendrite trunks and arms. Grain selection is therefore solely controlled by growth competition.

### **Growth**

Dendrite growth is driven by the chemical supersaturation  $\Omega_{\text{saturation}}$ , which is a dimensionless number proportional to the difference between the liquid composition at the dendrite tip and the melt composition far away from the tip. The higher the supersaturation, the faster the dendrite tip velocity. However, in the presence of a convective fluid, the chemical supersaturation is highly influenced by the intensity

and the direction of the flow with respect to the growth direction of the dendrites. In the current model, convection is central in studying freckle formation. Therefore, the purely diffusive Ivantsov relation used to determine the Peclet number  $Pe$  as function of the supersaturation, is replaced by a modified relation using a boundary layer correlation model that accounts for both the intensity and the misorientation of the liquid velocity with respect to the growth direction of the dendrites [Gandin et al. 2003]. The main parameters for this growth kinetics models are the Gibbs Thomson coefficient,  $\Gamma_{GT}$ , and the diffusion coefficient for Ga in In,  $D^l$ .

### Solidification path

The CA model gives the presence of the grains in the liquid as well as its growth undercooling. For coupling with macroscopic scale modelling, the fraction of phases needs to be fed back to the FE model. This is now done by accounting for the information provided by the CA model. Thus, the fraction of solid is no longer the consequence of a simple conversion of the temperature and composition assuming thermodynamic equilibrium. It also includes the solidification delay due to the kinetics of the development of the grains as detailed elsewhere in the work of Carozzani et al. [2013].

### Numerical method

Both the finite element mesh and the cellular automaton grid play a role in predicting freckles inasmuch as this type of defect originate from interplays between hydrodynamic instabilities on the scale of the dendrites and macroscopic flows defined by the geometry of the experimental cell [Shevchenko et al. 2013]. One has to respect a small maximum FE mesh size, comparable to the dendrite arm spacing. With such an element size, composition gradients giving rise to solutal buoyancy forces can be captured. This limits consequently the CA cell size, as a minimum number of cells is required in each finite element. In the array of simulations that will be presented in the next section, the value of  $\lambda_2$  was considered. We have chosen a fixed mesh element size of  $2\lambda_2$  and a CA cell size of  $\lambda_2/2$ . An average of 4 CA cells per unit length of a finite element is enough to accurately compute the development of the grain envelopes together with the solutal, thermal and mechanical interactions.

#### 4.6.2 Configuration

## 4.6. Meso-Macro prediction of channel segregates

---

**Table 4.3** – Summary of the simulations and the corresponding parameters for the CAFE cases, coupling macroscopic model with the grain structure model. Parameters are varied from (G1) low to (G2) high gradient, (R1) low to (R2) high cooling rate and (L0) no, (L1) low and (L2) high lateral cooling.

Case	Vertical gradient G [K mm <sup>-1</sup> ]	Cooling rate R [K s <sup>-1</sup> ]	Lateral cooling L (h <sub>ext</sub> , T <sub>ext</sub> ) [W m <sup>-2</sup> K <sup>-1</sup> , °C]	Initial temperature (T <sub>top</sub> , T <sub>bottom</sub> ) [°C]	Nucleation (n <sub>max</sub> , ΔT <sub>N</sub> , ΔT <sub>σ</sub> ) [m <sup>-2</sup> , °C, °C]
CAFE-G2R1L1	G2:1.5	R1:-0.01	L1:(20,0)	(58.25, 25.25)	(10 <sup>6</sup> , 1, 0.2)
CAFE-G1R1L1	G1:0.2	R1:-0.01	L1:(20,0)	(29.75, 25.25)	(10 <sup>6</sup> , 1, 0.2)
CAFE-G1R1L2	G1:0.2	R1:-0.01	L2:(500,0)	(29.75, 25.25)	(10 <sup>6</sup> , 1, 0.2)
CAFE-G2R2L1	G1:0.2	R2:-0.05	L1:(20,0)	(29.75, 25.25)	(10 <sup>6</sup> , 1, 0.2)

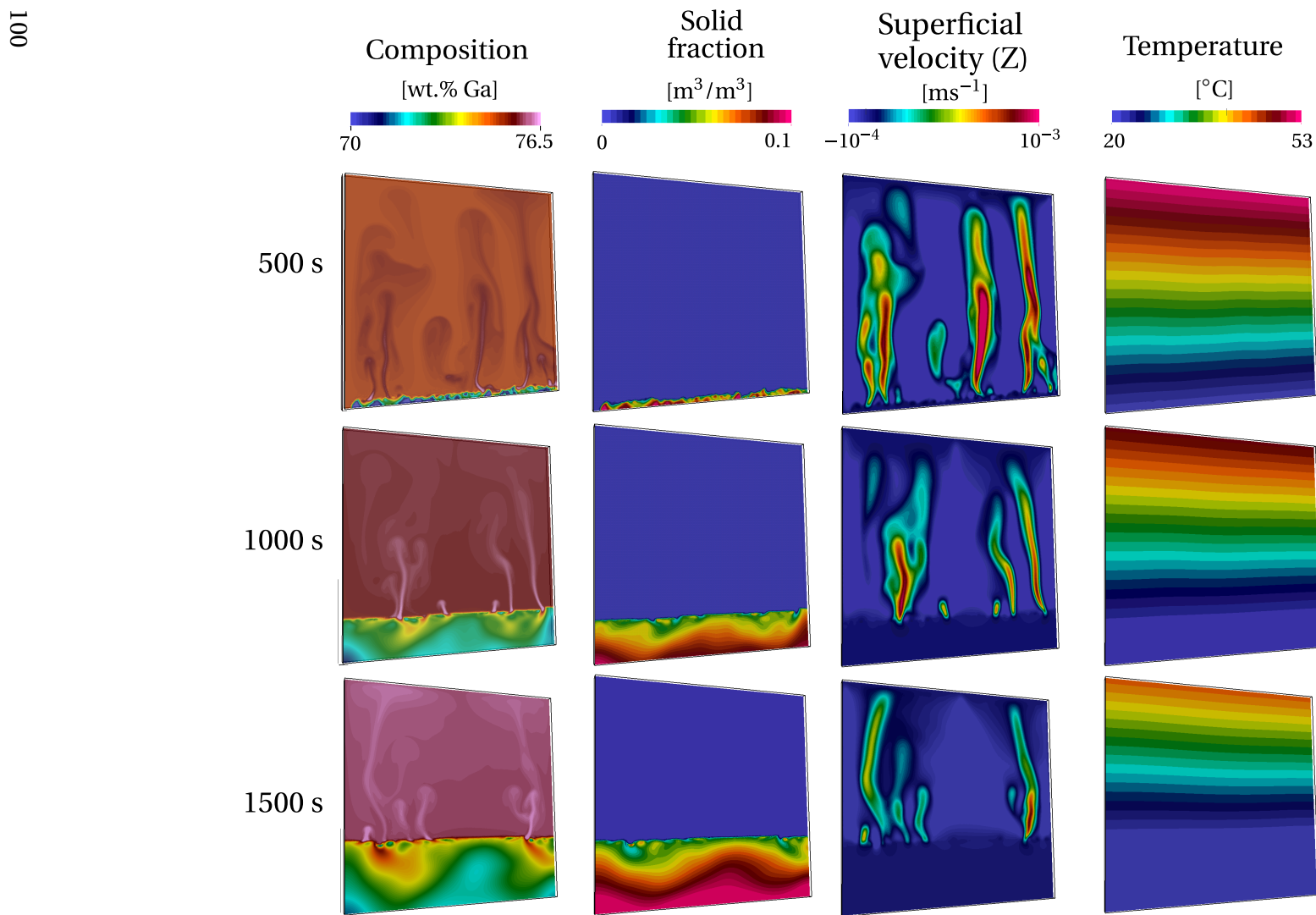


**Fig. 4.11 –** Simulation results for case CAFE-G2R1L1 showing maps of the average composition in gallium, the solid fraction, the superficial velocity field (vertical component) and the temperature, on a cut plane at the center of the cell at 500 s, 1000 s and 1500 s.

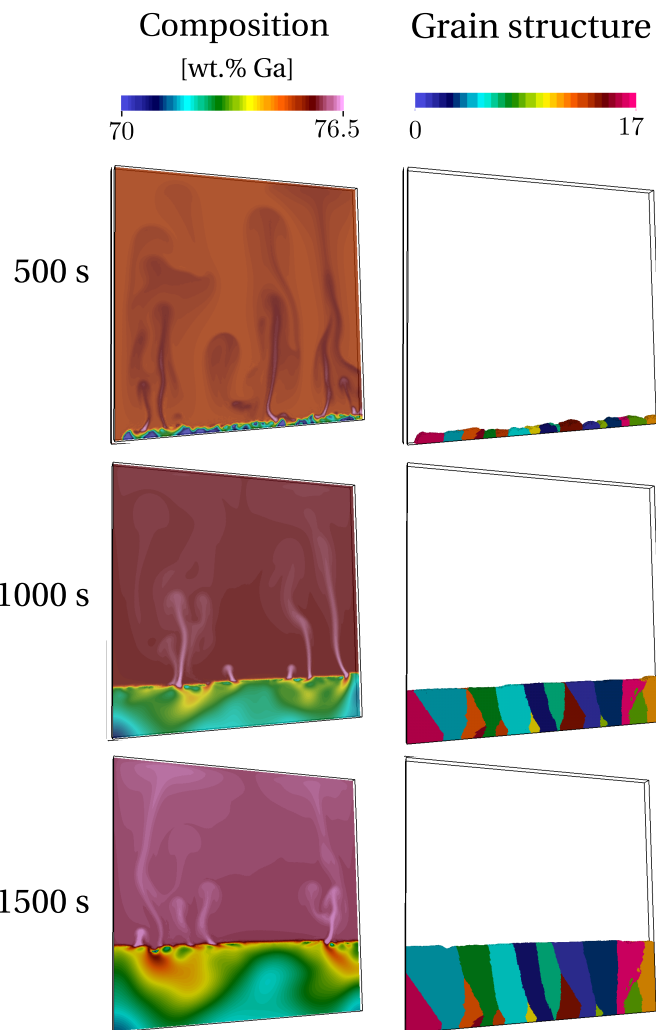


**Fig. 4.12** – Simulation results the predicted of mushy grain structure with the corresponding composition maps.

Knowing that the configuration in FE-G2R1L1 produces segregated channels, the same set of parameters is first used for case CAFE-G2R1L1 by adding the effect of the grain structure using the CAFE model. Results are accessible in [fig. 4.11](#) for comparison with [fig. 4.10](#). A striking difference is seen: the composition maps become more perturbed as shown by the formation of numerous plumes when coupling with grain structure is active. The growing front displayed on the grain structure at the right most column of [fig. 4.11](#) dictates the leading position of the mushy zone shown in the third column. Note that each color corresponds to one grain, with 17 grains having nucleated at the cell's bottom surface. However, comparison of the solid fraction maps between [fig. 4.10](#) and [fig. 4.11](#) at the same times reveals a delay in the growing front position.

Values of the nucleation parameters in [table 4.3](#) are such that few grains rapidly form

below the nominal liquidus isotherm. The delay is therefore not due to the nucleation undercooling but to the growth undercooling of the dendrite tips. It should be noticed that, the growth front driven by undercooling in [fig. 4.11](#) also forms with a higher initial solid fraction and hence larger solute segregation occurs at the front. This effect, together with instabilities of the composition field, is caused by a more perturbed fluid flow and more plumes as observed in CAFE-G2R1L1 compared to FE-G2R1L1. Such observations fit to the complicated fluid and solute flow patterns typically occurring in the experiments as shown in [fig. 4.13](#).

It becomes obvious that the consideration of grain structure and growth undercooling are vital to accurately simulate segregated channels formation in these experiments. The reasons for the instabilities are discussed hereinafter.

In the present 3D CAFE simulation, each grain shown in [fig. 4.12](#) is associated with a crystallographic orientation. The growth kinetics is only given for the  $\langle 100 \rangle$  crystallographic directions at the grain boundaries with the liquid. The CA growth model is based on the hypothesis that, in a quiescent liquid of uniform temperature distribution and composition, the grain envelop should reproduce an octahedral grain shape with main directions given by the six  $\langle 100 \rangle$  directions. In the present situation where complicated fields are present for temperature, composition and liquid velocity, each grain envelope with different crystallographic orientation adapts differently to its local environment. Thus, the local undercooling of the front varies everywhere. Such variations are within few degrees here, but this is sufficient to create irregularities on the growth front, as seen on the grain structure in [fig. 4.12](#). Apart from that, these variations are linked to the position of the instabilities for the chemical and liquid velocity fields, thus demonstrating the full coupling between the CA and FE models.

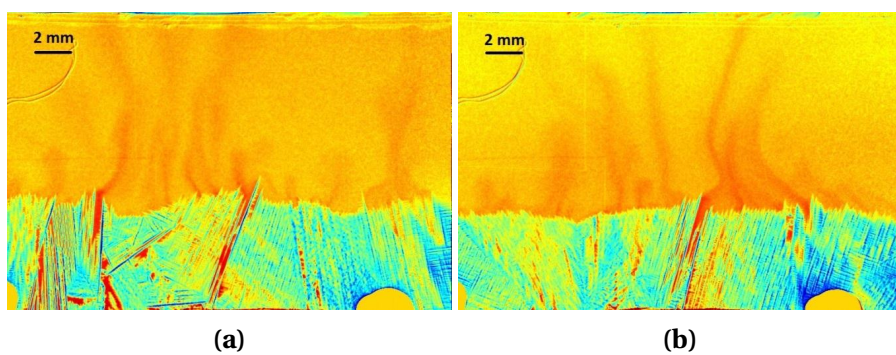


**Fig. 4.13** – Snapshots of dendritic structure and composition field obtained from two solidification experiments at a cooling rate  $R=-0.01 \text{ K s}^{-1}$  and temperature gradients of (a)  $G=1.1 \text{ K mm}^{-1}$  and (b)  $G=1.3 \text{ K mm}^{-1}$

### 4.6.3 Effect of vertical temperature gradient

The influence of diverse process parameters can now be considered in context of the grain structure. The effect of the vertical temperature gradient is shown by comparing the previous case CAFE-G2R1L1 with case CAFE-G1R1L1. The temperature gradient is decreased about 7 times here, from  $G_2=1.5 \text{ K mm}^{-1}$  to  $G_1=0.2 \text{ K mm}^{-1}$ . In fact, both cases share almost all traits with respect to flow patterns and velocity magnitude in the bulk. Main differences are yet seen regarding the dynamics of the plumes shown in [fig. 4.14](#).

In the case of a low temperature gradient ( $G_1$ ), the solidification front cannot maintain a shape as smooth as for the case of a large temperature gradient ( $G_2$ ): the solute gradient in the liquid of the mushy zone (basically following the lever rule approximation for a given temperature) decreases, leading to a lower gradient of the solutal buoyancy force. In turn, more solute accumulates close to the front and locally reduces the growth velocity, thus creating larger “valleys” or steps with higher solute content. The irregular geometry of the front is also influenced by the dendrite tip growth kinetics model. The velocity of the isotherms is the ratio of the cooling rate,  $R$ , to the temperature gradient,  $G$ . Consequently, the isotherm velocity in case  $G_1$  is larger than in  $G_2$ , since cooling rate,  $R_1$ , is the same in both cases. Moreover, because the dendrite tip velocity is a monotonously increasing function with the undercooling [[Gandin et al. 2003](#)], the latter for CAFE-G1R1L1 is larger than for CAFE-G2R1L1. Height differences of the growth front are proportional to the variations of the undercooling by the temperature gradient. Therefore, this forms larger steps on the growth front for case  $G_1$  compared to  $G_2$ .

The chimney extends deeper in the mushy zone when the temperature gradient increases. This is confirmed by both the simulation results shown in [fig. 4.14](#) as well as the experimental observations. Another remarkable phenomenon is also observed in the low gradient case: a “pulsing” mechanism in CAFE-G1R1L1 where a series of solute rich liquid pockets are observed one above the other. This corresponds to a repeated and localized strong spatial variation of the liquid velocity field outside the mushy zone, regularly thrusting away small plumes. These pulses are roughly similar to each other in size and exit speed, creating thus a very regular pattern during some time. In the case of a high temperature gradient (case CAFE-G2R1L1) this phenomenon is barely seen. In fact, the pattern shown in [fig. 4.14](#) is more typical, with continuous plume rising from the mushy zone and reaching the top of the domain. However, such regular plume is the initial and final pattern seen for low gradient before the pulsing regime. Similar observations have been made in the experiments too. [Figure 4.16a](#) displays the phenomenon of the “pulsing” plumes, which could be explained by the

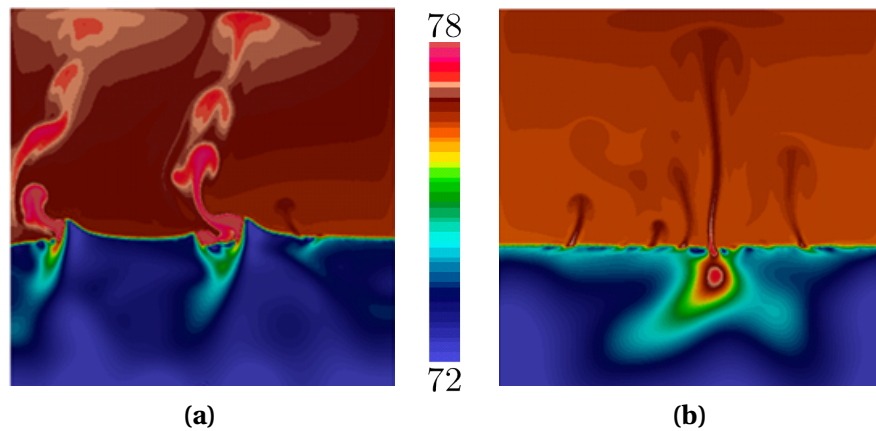


**Fig. 4.14** – Average composition maps for CAFE-G1R1L1 at time 1060 s and CAFE-G2R1L1 at time 1845 s.



**Fig. 4.15** – Snapshot of the pulsing mechanism coming from a groove shape in the mushy (check animation in the PDF file).

following mechanisms. The permeability of the mushy zone and the narrow gap of the solidification cell obstruct the feeding of the plumes by solute. A critical solute concentration has to be accumulated at a specific location in order to trigger the formation of a rising plume. An interim drop of the solute concentration below such a threshold would interrupt the plume. Flow instabilities can be another reason for the peculiar shape of the plumes. [Figure 4.16b](#) shows a pronounced continuous plume. The same plume can be seen a few seconds later in [fig. 4.16c](#). The plume structure becomes unstable; one can observe an indentation of streamlines followed by a mixing of rising solute-rich liquid with descending In-rich fluid. This mechanism also causes a non-continuous structure of the plumes.

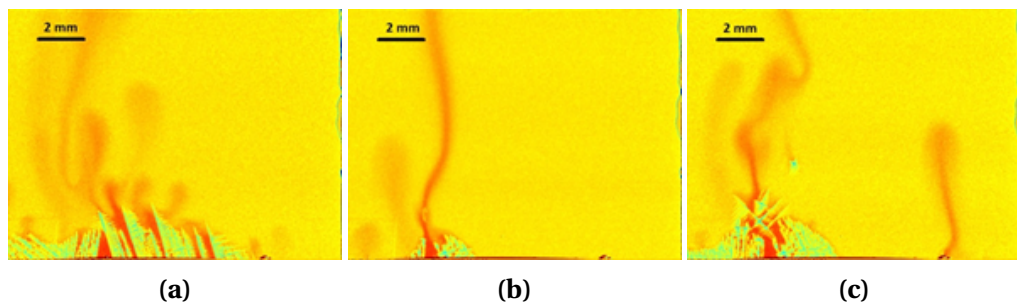


**Fig. 4.16** – Snapshots of dendrite structure and composition field from two solidification experiments conducted at a cooling rate  $R=-0.01 \text{ K s}^{-1}$  and a temperature gradient  $=1 \text{ K mm}^{-1}$ : (a) “pulsing” plumes, (b) continuous plume, (c) upcoming plume instability.

### 4.6.4 Effect of cooling rate

The next parameter studied is the cooling rate, corresponding to case CAFE-G1R2L1. A snapshot of the composition map and the corresponding vertical component of the velocity field are given in [fig. 4.17](#). We see a similarity with case CAFE-G1R1L1 in [fig. 4.14a](#) with respect to the buckled interface between the liquid and the mushy zone as well a plume pulsing effect when a low temperature gradient is applied. On the other hand, segregation inside the mush is more irregular with more pronounced patterns reaching a larger depth. One could distinguish alternating V and A shapes patterns in the mushy zone. As for case CAFE-G1R1L1, these patterns are created by a network of pulsing plumes formed by the steps created on the delocalized growth front due to the low temperature gradient. However, these considerations are not sufficient to explain the shape of the growth front. The reason for the protuberances created at the tips of the V shape is the presence of a descending bulk liquid with a low composition seen by the growth front. It infers that favorable growth conditions are created for a higher working temperature since the dendrite tip undercooling de-

creases for facing liquid flow and a lower composition; the growth rate is given by the isotherm velocity. The growth front thus adjusts its position to catch up with the corresponding isotherm, the latter being located at the tips of the V shape, i.e. the outmost advanced position of the growth front. It also means that the V shape angle depends on the size and intensity of the convection loops above the front. When the steps are formed on the growth front, the plumes exiting the mushy zone follow a direction normal to the front. They are inclined towards each other above the V shape. As a result, they may join and form a larger plume as seen in CAFE-G1R1L1 ([fig. 4.14a](#)), thus forming larger and more stable segregated channels. The other observation in [fig. 4.17](#) is the existence of stable regions of the growth front. For instance, this is seen in between the two V shape forming or on the right hand side of the cell. The reason

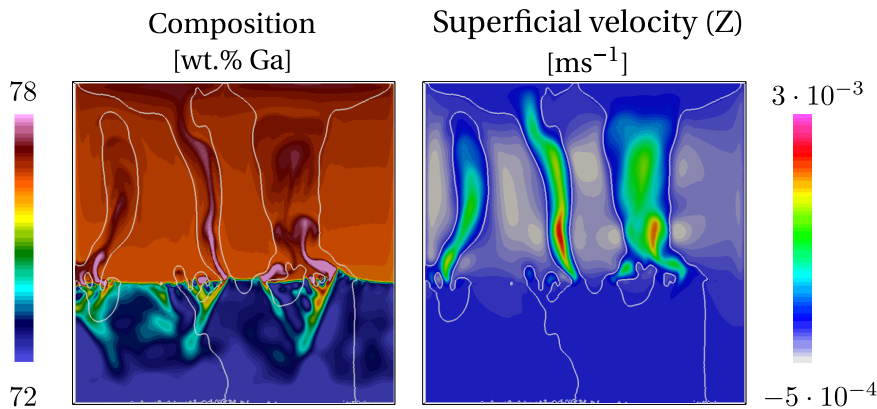


**Fig. 4.17** – Average fields inside the cell for case CAFE-G1R2L1 at 350 s. The white contour identifies the zero velocity limit for the vertical component of the velocity field

for this stability is the inversion of the composition gradient located ahead. Animation shows that solute coming from the top of the cell is responsible for this accumulation, creating a layering that provides a stabilization effect above the mushy zone. This is verified by the vertical component of the average velocity also made available in [fig. 4.17](#). It is negative outside the path of the plumes. A resulting concurrent effect is the formation of the A shape segregates in between the V shape patterns seen in [fig. 4.17](#). Finally, it can be observed that these patterns are sustained longer compared to [fig. 4.14](#) CAFE-G1R1L1 because, at high cooling rate, the flow in the mushy zone is decreased due to a faster solidification. This is the same effect as described for the large gradient configuration in CAFE-G2R1L1 ([fig. 4.14b](#)). It is not clear how these observations could be compared with the A and V shapes segregates reported for steel ingots [[Pickering 2013](#)]. Despite the fact that macrosegregation is the main phenomenon leading to these patterns, there has not been a clear explanation yet in the literature for their formation. However, for steel casting, the A and V patterns

are believed to form concomitantly. Further investigations would thus be required to quantify the consequences of thermosolutal instabilities simulated here for an In-75 wt.% Ga alloy and check their possible correlation with experimental observations in steel casting.

#### 4.6.5 Effect of lateral temperature gradient

The previous simulations show the effect of cooling rate and temperature gradient on the survival of segregation patterns deep in the mushy zone. Another simulation is performed by increasing the cooling rate using higher heat flux extracted from the vertical side boundaries. This is achieved in case CAFE-G1R1L2 where the heat transfer coefficient reaches  $500 \text{ W m}^{-2} \text{ K}^{-1}$ . As a consequence of the large cooling from the sides, the temperature gradient is no longer vertical. A distinct flow due to thermal buoyancy is created, driving a cold liquid downwards near the sides of the cell. Under the influence of these 2 main convection loops, all segregation plumes tend to regroup in the middle of the domain, forming a larger central plume, as seen in the composition map at 450 s in [fig. 4.18](#). However, this regime occurs at times earlier than 500 s, where the effect of thermally induced buoyancy forces is prevailing, feeding the convection loops. Approximately 500 s later, the mushy zone has extended, favouring the segregation mechanical forces i.e.  $\rho_{\text{ref}} (1 - \beta_{\langle w \rangle^l} \Delta \langle w \rangle^l) \vec{g}$ , rather than the thermal mechanical forces,  $\rho_{\text{ref}} (1 - \beta_T \Delta T) \vec{g}$ . [Figure 4.18](#) shows the correspond-

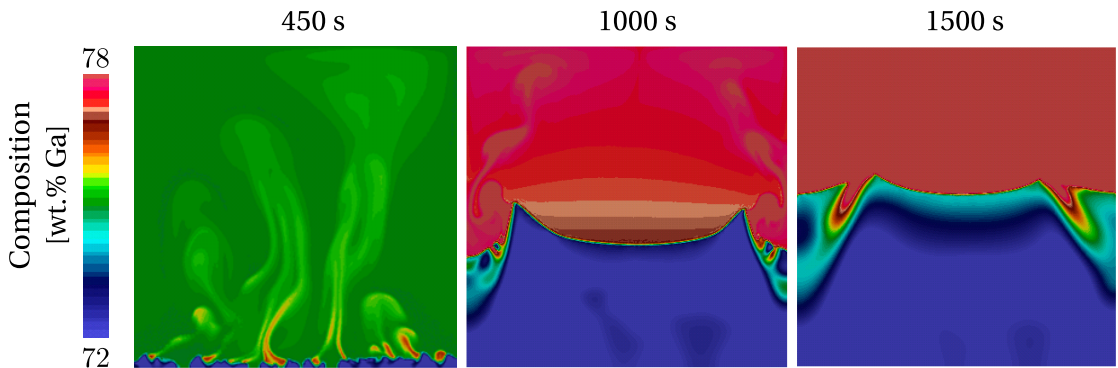


**Fig. 4.18** – 2D cut plane of the average composition inside the cell for case CAFE-G1R1L2 at the following time increments: 450 s, 1000 s and 1500 s.

ing composition maps with stable chimneys at about 1000 s that also remain at 1500 s. The solidification front then tends to form a concave shape at the center of the cell, thus partially revealing the form of the isotherms toward the cell center. The stable pattern in the center is similar to the plateau seen at the center, between the A-shapes in [fig. 4.14](#) and [fig. 4.17](#). As stated before, it is an inactive region with respect

to plume initiation due to the inversion of the solute composition gradient. In other words, the high gallium concentration at the top of cell causes indium, which is the heavier species, to accumulate and be partially trapped between the mushy walls, thus creating a stable flow configuration. Outside of the plateau, 2 plumes are observed from the prominent instabilities of the growth front, adopting diverging directions. This is also observed at the center of the cell in [fig. 4.17](#) on each side of the A-shape segregate. These plumes in [fig. 4.18](#) lead to the formation of two stable channels. The corresponding situation in the experiment is shown in [fig. 4.19](#). The chimneys on both sides and the plateau in between can be clearly recognised. The additional cooling at the side walls produces two flow vortices between the side wall and the strong convective plumes above the chimneys. The central part of the sample remains almost unaffected by the additionally driven thermal convection. This area is characterised by the occurrence of a number of smaller convective plumes.

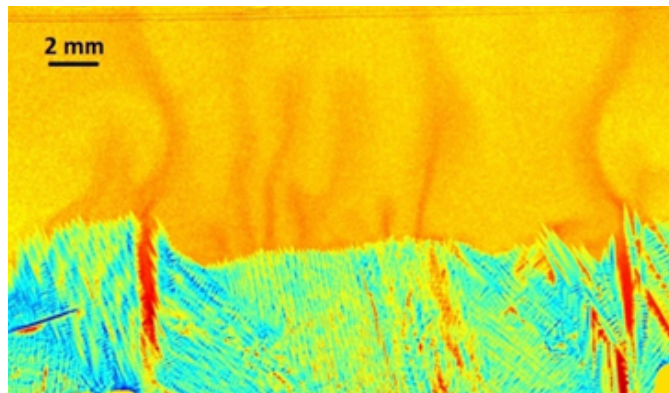


**Fig. 4.19** – Snapshot of dendritic structure and composition field from a solidification experiment recorded at 1000 s for a cooling rate  $R=-0.01 \text{ Ks}^{-1}$  and a temperature gradient  $G=-1 \text{ Kmm}^{-1}$ .

#### 4.6.6 Mono-grain freckles

All CAFE simulations were performed considering a normal classic heterogeneous nucleation at the surface of the mould where the metal is cooled down. However, as the number of grains is not negligible, the subsequent fluid-structure interaction between dendrites, simply represented by an isotropic permeability and the interdendritic flow cannot be easily interpreted. Therefore, one may consider simpler solidification cases like a mono-grain growth. This ideal situation is not always experimentally viable: either the mould surface is not perfectly smooth, and therefore nucleation can be triggered by a wetting mechanism, or the metal contains a certain level of impurity which can trigger nucleation heterogeneously in the liquid bulk. Regardless of this

#### 4.6. Meso-Macro prediction of channel segregates

experimental limitation, this type of simulations allows simpler understanding as the grain growth is not disturbed by another neighbouring grain, it grows while exclusively interacting with the liquid phase.

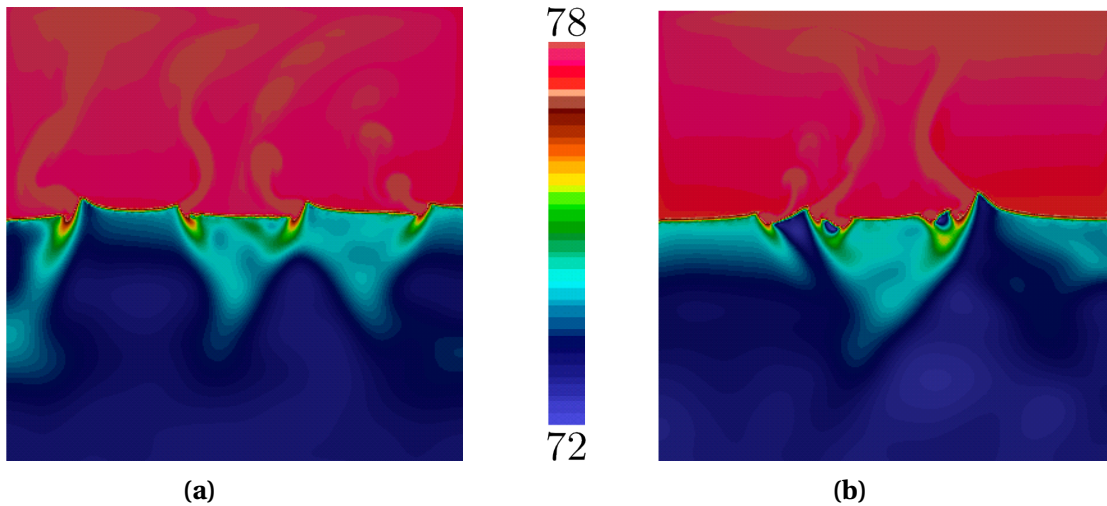


**Fig. 4.20** – Snapshots of mono-grain solidification showing the average composition in gallium predicted by the CAFE approach. Two orientation scenarios are considered where a) the grain is upright with a Euler angle of  $(90^\circ, 0^\circ, 0^\circ)$  or b) the grain is tilted with a Euler angle of  $(90^\circ, 30^\circ, 0^\circ)$  (check animation in the PDF file).

**Résumé chapitre 4**

# Bibliography

## [Andersson et al. 2002]

Andersson, J.-O., Helander, T., Höglund, L., Shi, P., and Sundman, B. (2002). “Thermo-Calc & DICTRA, computational tools for materials science”. *Calphad*, 26 (2), pp. 273–312. URL: <http://www.sciencedirect.com/science/article/pii/S0364591602000378> (cited on pages 63, 65, 66, 92).

## [Arnold et al. 1984]

Arnold, D. N., Brezzi, F., and Fortin, M. (1984). “A stable finite element for the stokes equations”. *CALCOLO*, 21 (4), pp. 337–344. URL: <http://link.springer.com/article/10.1007/BF02576171> (cited on page 73).

## [Auburtin et al. 2000]

Auburtin, P., Wang, T., Cockcroft, S. L., and Mitchell, A. (2000). “Freckle formation and freckle criterion in superalloy castings”. *Metallurgical and Materials Transactions B*, 31 (4), pp. 801–811. URL: <http://link.springer.com/article/10.1007/s11663-000-0117-9> (cited on page 96).

## [Auburtin 1998]

Auburtin, P. B. L. (1998). “Determination of the influence of growth front angle on freckle formation in superalloys”. PhD thesis. Vancouver, BC, Canada: University of British Columbia. URL: [https://circle.ubc.ca/bitstream/handle/2429/8676/ubc\\_1998-345084.pdf?sequence=1](https://circle.ubc.ca/bitstream/handle/2429/8676/ubc_1998-345084.pdf?sequence=1) (cited on page 87).

## [Babuška 1971]

Babuška, I. (1971). “Error-bounds for finite element method”. *Numerische Mathematik*, 16 (4), pp. 322–333. URL: <http://link.springer.com/article/10.1007/BF02165003> (cited on page 73).

## [Barbosa and Hughes 1991]

Barbosa, H. J. C. and Hughes, T. J. R. (1991). “The finite element method with Lagrange multipliers on the boundary: circumventing the Babuška-Brezzi condition”. *Computer Methods in Applied Mechanics and Engineering*, 85 (1), pp. 109–128. URL: <http://www.sciencedirect.com/science/article/pii/004578259190125P> (cited on page 73).

## [Beckermann et al. 2000]

Beckermann, C., Gu, J. P., and Boettinger, W. J. (2000). “Development of a freckle predictor via rayleigh number method for single-crystal nickel-base superalloy castings”. *Metallurgical and Materials Transactions A*, 31 (10), pp. 2545–2557. URL: <http://link.springer.com/article/10.1007/s11661-000-0199-7> (cited on pages 82, 87).

## Bibliography

---

### [Bellet et al. 2009]

Bellet, M., Combeau, H., Fautrelle, Y., Gobin, D., Rady, M., Arquis, E., Budenkova, O., Dussoubs, B., Duterrail, Y., Kumar, A., Gandin, C. A., Goyeau, B., Mosbah, S., and Založnik, M. (2009). "Call for contributions to a numerical benchmark problem for 2D columnar solidification of binary alloys". *International Journal of Thermal Sciences*, 48 (11), pp. 2013–2016. URL: <http://www.sciencedirect.com/science/article/pii/S129007290900177X> (cited on page 48).

### [Boden et al. 2008]

Boden, S., Eckert, S., Willers, B., and Gerbeth, G. (2008). "X-Ray Radioscopic Visualization of the Solutal Convection during Solidification of a Ga-30 Wt Pct In Alloy". *Metallurgical and Materials Transactions A*, 39 (3), pp. 613–623. URL: <http://link.springer.com/article/10.1007/s11661-007-9462-5> (cited on page 89).

### [Brezzi 1974]

Brezzi, F. (1974). "On the existence, uniqueness and approximation of saddle-point problems arising from lagrangian multipliers". *ESAIM: Mathematical Modelling and Numerical Analysis - Modélisation Mathématique et Analyse Numérique*, 8 (R2), pp. 129–151. URL: <https://eudml.org/doc/193255> (cited on page 73).

### [Carozzani et al. 2012]

Carozzani, T., Digonnet, H., and Gandin, C.-A. (2012). "3D CAFE modeling of grain structures: application to primary dendritic and secondary eutectic solidification". *Modelling and Simulation in Materials Science and Engineering*, 20 (1), p. 015010. URL: <http://iopscience.iop.org/0965-0393/20/1/015010> (cited on page 97).

### [Carozzani et al. 2014]

Carozzani, T., Gandin, C.-A., and Digonnet, H. (2014). "Optimized parallel computing for cellular automaton-finite element modeling of solidification grain structures". *Modelling and Simulation in Materials Science and Engineering*, 22 (1), p. 015012. URL: <http://iopscience.iop.org/0965-0393/22/1/015012> (cited on page 97).

### [Carozzani et al. 2013]

Carozzani, T., Gandin, C.-A., Digonnet, H., Bellet, M., Zaidat, K., and Fautrelle, Y. (2013). "Direct Simulation of a Solidification Benchmark Experiment". *Metallurgical and Materials Transactions A*, 44 (2), pp. 873–887. URL: <http://link.springer.com/article/10.1007/s11661-012-1465-1> (cited on pages 48, 81, 97, 98).

### [Copley et al. 1970]

Copley, S. M., Giamei, A. F., Johnson, S. M., and Hornbecker, M. F. (1970). "The origin of freckles in unidirectionally solidified castings". *Metallurgical Transactions*, 1 (8), pp. 2193–2204. URL: <http://link.springer.com/article/10.1007/BF02643435> (cited on page 86).

### [Desbiolles et al. 2003]

Desbiolles, J.-L., Thévoz, P., Rappaz, M., and Stefanescu, D. (2003). "Micro-Macrosegregation Modeling in Casting: A Fully Coupled 3D Model". TMS Publ., pp. 245–252 (cited on page 89).

### [Doré et al. 2000]

Doré, X., Combeau, H., and Rappaz, M. (2000). "Modelling of microsegregation in ternary alloys: Application to the solidification of Al–Mg–Si". *Acta Materialia*, 48 (15), pp. 3951–3962. URL: <http://www.sciencedirect.com/science/article/pii/S1359645400001774> (cited on page 48).

**[Du et al. 2007]**

Du, Q., Eskin, D. G., and Katgerman, L. (2007). "Modeling Macrosegregation during Direct-Chill Casting of Multicomponent Aluminum Alloys". *Metallurgical and Materials Transactions A*, 38 (1), pp. 180–189. URL: <http://link.springer.com/article/10.1007/s11661-006-9042-0> (cited on page 48).

**[Felicelli et al. 1991]**

Felicelli, S. D., Heinrich, J. C., and Poirier, D. R. (1991). "Simulation of freckles during vertical solidification of binary alloys". *Metallurgical Transactions B*, 22 (6), pp. 847–859. URL: <http://link.springer.com/article/10.1007/BF02651162> (cited on pages 84, 89).

**[Felicelli et al. 1998]**

Felicelli, S. D., Poirier, D. R., and Heinrich, J. C. (1998). "Modeling freckle formation in three dimensions during solidification of multicomponent alloys". *Metallurgical and Materials Transactions B*, 29 (4), pp. 847–855. URL: <http://link.springer.com/article/10.1007/s11663-998-0144-5> (cited on page 89).

**[Flemings and Nereo 1967]**

Flemings, M. C. and Nereo, G. E. (1967). "Macrosegregation: Part I". *Transactions of the Metallurgical Society of AIME*, 239, pp. 1449–1461 (cited on page 87).

**[Flemings and Nereo 1968]**

Flemings, M. C. and Nereo, G. E. (1968). "Macrosegregation: Part III". *Transactions of the Metallurgical Society of AIME*, 242, pp. 50–55 (cited on page 87).

**[Flemings et al. 1968]**

Flemings, M. C., Mehrabian, R., and Nereo, G. E. (1968). "Macrosegregation: Part II". *Transactions of the Metallurgical Society of AIME*, 242, pp. 41–49 (cited on page 87).

**[Gandin 2000]**

Gandin, C. A. (2000). "From constrained to unconstrained growth during directional solidification". *Acta Materialia*, 48 (10), pp. 2483–2501. URL: <http://www.sciencedirect.com/science/article/pii/S1359645400000707> (cited on pages 58, 70).

**[Gandin et al. 2003]**

Gandin, C. A., Guillemot, G., Appolaire, B., and Niane, N. T. (2003). "Boundary layer correlation for dendrite tip growth with fluid flow". *Materials Science and Engineering: A*, 342 (1–2), pp. 44–50. URL: <http://www.sciencedirect.com/science/article/pii/S0921509302002617> (cited on pages 98, 103).

**[Genereux and Borg 2000]**

Genereux, P. D. and Borg, C. A. (2000). "Characterization of Freckles in a High Strength Wrought Nickel Superalloy". Warrendale, PA: K.A. Green, M. McLean, S. Olson, J.J. Schirra, TMS (The Minerals, Metals, and Materials Society), pp. 19–27. URL: [http://www.tms.org/superalloys/10.7449/2000/Superalloys\\_2000\\_19\\_27.pdf](http://www.tms.org/superalloys/10.7449/2000/Superalloys_2000_19_27.pdf) (cited on page 87).

**[Giamei and Kear 1970]**

Giamei, A. F. and Kear, B. H. (1970). "On the nature of freckles in nickel base superalloys". *Metallurgical Transactions*, 1 (8), pp. 2185–2192. URL: <http://link.springer.com/article/10.1007/BF02643434> (cited on page 87).

## Bibliography

---

### [Gouttebroze 2005]

Gouttebroze, S. (2005). "Modélisation 3d par éléments finis de la macroségrégation lors de la solidification d'alliages binaires". PhD thesis. École Nationale Supérieure des Mines de Paris. URL: <https://pastel.archives-ouvertes.fr/pastel-00001885/document> (cited on page 79).

### [Guo and Beckermann 2003]

Guo, J. and Beckermann, C. (2003). "Three-Dimensional Simulation of Freckle Formation During Binary Alloy Solidification: Effect of Mesh Spacing". *Numerical Heat Transfer, Part A: Applications*, 44 (6). <http://dx.doi.org/10.1080/716100512>, pp. 559–576. URL: <http://user.engineering.uiowa.edu/~becker/documents.dir/GuoFreckle.pdf> (cited on page 89).

### [Hachani et al. 2012]

Hachani, L., Saadi, B., Wang, X. D., Nouri, A., Zaidat, K., Belgacem-Bouzida, A., Ayouni-Derouiche, L., Raimondi, G., and Fautrelle, Y. (2012). "Experimental analysis of the solidification of Sn-3 wt.%Pb alloy under natural convection". *International Journal of Heat and Mass Transfer*, 55 (7–8), pp. 1986–1996. URL: <http://www.sciencedirect.com/science/article/pii/S0017931011007009> (cited on page 81).

### [Hachem et al. 2010]

Hachem, E., Rivaux, B., Kloczko, T., Digonnet, H., and Coupez, T. (2010). "Stabilized finite element method for incompressible flows with high Reynolds number". *Journal of Computational Physics*, 229 (23), pp. 8643–8665. URL: <http://www.sciencedirect.com/science/article/pii/S0021999110004237> (cited on page 75).

### [Hachem 2009]

Hachem, E. (2009). "Stabilized finite element method for heat transfer and turbulent flows inside industrial furnaces". PhD Thesis. École Nationale Supérieure des Mines de Paris. URL: <https://tel.archives-ouvertes.fr/tel-00443532> (cited on page 75).

### [Hebditch and Hunt 1974]

Hebditch, D. J. and Hunt, J. D. (1974). "Observations of ingot macrosegregation on model systems". *Metallurgical Transactions*, 5 (7), pp. 1557–1564. URL: <http://link.springer.com/article/10.1007/BF02646326> (cited on page 81).

### [Karagadde et al. 2014]

Karagadde, S., Yuan, L., Shevchenko, N., Eckert, S., and Lee, P. D. (2014). "3-D microstructural model of freckle formation validated using in situ experiments". *Acta Materialia*, 79, pp. 168–180. URL: <http://www.sciencedirect.com/science/article/pii/S1359645414004984> (cited on page 96).

### [Kohler 2008]

Kohler, F. (2008). "Peritectic solidification of Cu-Sn alloys: microstructure competition at low speed". PhD Thesis. EPFL (cited on page 89).

### [Lee et al. 2002]

Lee, P. D., Atwood, R. C., Dashwood, R. J., and Nagaumi, H. (2002). "Modeling of porosity formation in direct chill cast aluminum-magnesium alloys". *Materials Science and Engineering: A*, 328 (1–2), pp. 213–222. URL: <http://www.sciencedirect.com/science/article/pii/S0921509301016872> (cited on page 96).

### [Liu 2005]

Liu, W. (2005). "Finite Element Modelling of Macrosegregation and Thermomechanical Phenomena in Solidification Processes". PhD thesis. École Nationale Supérieure des Mines de Paris. URL: <http://pastel.archives-ouvertes.fr/pastel-00001339> (cited on page 79).

### [Pickering 2013]

Pickering, E. J. (2013). "Macrosegregation in Steel Ingots: The Applicability of Modelling and Characterisation Techniques". *ISIJ International*, 53 (6), pp. 935–949 (cited on pages 87, 106).

### [Pollock and Murphy 1996]

Pollock, T. M. and Murphy, W. H. (1996). "The breakdown of single-crystal solidification in high refractory nickel-base alloys". *Metallurgical and Materials Transactions A*, 27 (4), pp. 1081–1094. URL: <http://link.springer.com/article/10.1007/BF02649777> (cited on page 96).

### [Ramirez and Beckermann 2003]

Ramirez, J. C. and Beckermann, C. (2003). "Evaluation of a rayleigh-number-based freckle criterion for Pb-Sn alloys and Ni-base superalloys". *Metallurgical and Materials Transactions A*, 34 (7), pp. 1525–1536. URL: <http://link.springer.com/article/10.1007/s11661-003-0264-0> (cited on pages 87, 89, 96).

### [Rappaz et al. 2003]

Rappaz, M., Bellet, M., and Deville, M. (2003). *Numerical Modeling in Materials Science and Engineering*. Springer Series in Computational Mathematics. Springer Berlin Heidelberg (cited on pages 49, 54).

### [Rivaux 2011]

Rivaux, B. (2011). "Simulation 3D éléments finis des macroségrégations en peau induites par déformations thermomécaniques lors de la solidification d'alliages métalliques". PhD Thesis. École Nationale Supérieure des Mines de Paris. URL: <http://pastel.archives-ouvertes.fr/pastel-00637168> (cited on pages 75, 79).

### [Schneider et al. 1997]

Schneider, M. C., Gu, J. P., Beckermann, C., Boettinger, W. J., and Kattner, U. R. (1997). "Modeling of micro- and macrosegregation and freckle formation in single-crystal nickel-base superalloy directional solidification". *Metallurgical and Materials Transactions A*, 28 (7), pp. 1517–1531. URL: <http://link.springer.com/article/10.1007/s11661-997-0214-3> (cited on page 87).

### [Shevchenko et al. 2013]

Shevchenko, N., Boden, S., Gerbeth, G., and Eckert, S. (2013). "Chimney Formation in Solidifying Ga-25wt pct In Alloys Under the Influence of Thermosolutal Melt Convection". *Metallurgical and Materials Transactions A*, 44 (8), pp. 3797–3808. URL: <http://link.springer.com/article/10.1007/s11661-013-1711-1> (cited on pages 87, 89–91, 96, 98).

### [Süli 2000]

Süli, E. (2000). *Lecture Notes on Finite Element Methods for Partial Differential Equations* (cited on page 52).

### [Swaminathan and Voller 1993]

Swaminathan, C. R. and Voller, V. R. (1993). "On The Enthalpy Method". *International Journal of Numerical Methods for Heat & Fluid Flow*, 3 (3), pp. 233–244. URL: <http://www.emeraldinsight.com/journals.htm?articleid=1665561&show=abstract> (cited on page 48).

## Bibliography

---

### [TCBIN 2006]

TCBIN (2006). *TCBIN: TC Binary Solutions Database*. Stockholm, SE (cited on page 92).

### [TCFE6 2010]

TCFE6 (2010). *TCFE6: a thermodynamic database for different kinds of steels and Fe-based alloys*. Stockholm, SE. URL: <http://goo.gl/qiD3kE> (cited on pages 63, 65, 66).

### [Tezduyar et al. 1992]

Tezduyar, T. E., Mittal, S., Ray, S. E., and Shih, R. (1992). "Incompressible flow computations with stabilized bilinear and linear equal-order-interpolation velocity-pressure elements". *Computer Methods in Applied Mechanics and Engineering*, 95 (2), pp. 221–242. URL: <http://www.sciencedirect.com/science/article/pii/0045782592901416> (cited on pages 75, 79).

### [Tezduyar and Osawa 2000]

Tezduyar, T. E. and Osawa, Y. (2000). "Finite element stabilization parameters computed from element matrices and vectors". *Computer Methods in Applied Mechanics and Engineering*, 190 (3–4), pp. 411–430. URL: <http://www.sciencedirect.com/science/article/pii/S0045782500002115> (cited on page 79).

### [Thuiniet and Combeau 2004]

Thuiniet, L. and Combeau, H. (2004). "Prediction of macrosegregation during the solidification involving a peritectic transformation for multicomponent steels". *Journal of Materials Science*, 39 (24), pp. 7213–7219. URL: <http://link.springer.com/article/10.1023/B%3AJMSC.0000048734.34597.1e> (cited on page 48).

### [Yuan and Lee 2012]

Yuan, L. and Lee, P. D. (2012). "A new mechanism for freckle initiation based on microstructural level simulation". *Acta Materialia*, 60 (12), pp. 4917–4926. URL: <http://www.sciencedirect.com/science/article/pii/S1359645412003205> (cited on page 96).

### [Zabaras and Samanta 2004]

Zabaras, N. and Samanta, D. (2004). "A stabilized volume-averaging finite element method for flow in porous media and binary alloy solidification processes". *International Journal for Numerical Methods in Engineering*, 60 (6), pp. 1103–1138. URL: <http://onlinelibrary.wiley.com/doi/10.1002/nme.998/abstract> (cited on page 79).